Tracking exocytic vesicle movements with MSP-tracker/viewer reveals the spatial control of secretion in epithelial cells.

Jennifer H. Richens[1*], Mariia Dmitrieva[2*], Helen L. Zenner[1*], Nadine Muschalik[3], Richard Butler[1], Jade Glashauser[4], Carolina Camelo[4], Stefan Luschnig[4], Sean Munro[3], Jens Rittscher[2,5] and Daniel St Johnston[1].

[*]equal contributions

[1] The Gurdon Institute and the Department of Genetics, University of Cambridge Tennis court Rd, Cambridge CB2 1QN, United Kingdom

[2] Institute of Biomedical Engineering (IBME), Department of Engineering Science and the Big Data Institute, Li Ka Shing Centre for Health Information and Discovery, University of Oxford, Oxford, UK

[3]MRC-Laboratory of Molecular Biology, Francis Crick Avenue, Cambridge Biomedical Campus, Cambridge, CB2 0QH, UK

[4]Institute of Integrative Cell Biology and Physiology, Cells in Motion (CiM) Interfaculty Centre, University of Münster, D-48149 Münster, Germany

[5] Ludwig Institute for Cancer Research, Nuffield Department of Clinical Medicine, University of Oxford, Oxford, UK

Abstract

Understanding how specific secretory cargoes are targeted to distinct domains of the plasma membrane in epithelial cells requires analysing the trafficking of post-Golgi vesicles to their sites of secretion. Here, we introduce an interactive vesicle tracking framework, the multiscale particle tracker and viewer, that exploits developments in computer vision and deep learning to determine vesicle trajectories in noisy cellular environments without the need for extensive training data. We analysed the movements of secreted cargoes in the *Drosophila* follicular epithelium ex vivo with high temporal and spatial resolution and found that MSP-tracker outperformed other tracking software. Using the RUSH (retention using selective hooks) system to synchronously release cargoes from the endoplasmic reticulum, we followed the movements the microvillar protein, Cadherin 99C, to the plasma membrane. A dominant slow dynein mutant reduces the speed of apical Cad99C movements, demonstrating that dynein transports Cad99C vesicles to the apical cortex. Furthermore, both the dynein mutant and microtubule depolymerisation cause lateral Cad99C secretion. Thus, microtubule organisation plays a central role in targeting secretion, suggesting that *Drosophila* does not have distinct apical versus basolateral vesicle fusion machinery. Imaging the extracellular matrix protein (ECM) proteins, Nidogen and Collagen IV revealed that Nidogen vesicles undergo planar-polarised transport to the leading edge of follicle cells as they migrate over the ECM, whereas Collagen is secreted at trailing edges. The follicle cells therefore secrete different ECM components at opposite sides of the cell, revealing that the secretory pathway is more spatially organised than previously thought.

Introduction

Many tissues and organs are composed of tubes or sheets of polarised epithelial cells that act as barriers between internal compartments or between the inside and outside of the body. A key function of epithelia is to control the passage of ions, solutes and nutrients from one side of the epithelium to the other and this requires localisation of ion channels and

transporters to either the apical or basolateral domains of the plasma membrane and the formation of lateral occluding junctions that act as barriers to paracellular transport [1,2]. In addition, many epithelia secrete specific factors from their apical or basal surfaces. To perform these diverse functions, epithelial cells must target secreted and transmembrane proteins to either the apical or basolateral plasma membrane.

Many secreted and transmembrane proteins are localised to the correct domain by polarised exocytosis. In this direct pathway, newly synthesised proteins traffic through the endoplasmic reticulum (ER) and Golgi to the trans-Golgi network (TGN), where they are sorted into post-Golgi carriers that move to and then fuse with the appropriate membrane [3,4]. Other proteins are localised by different mechanisms, however, such as diffusion and trapping or secretion to the opposite membrane, followed by polarised endocytosis and recycling. The direct route can be distinguished from indirect localisation mechanisms by following newly-synthesized protein molecules on their first passage to the plasma membrane by blocking them in the ER or Golgi and then releasing them, which is possible for specific proteins, such as a temperature-sensitive form of VSV-G protein and *Drosophila* Rhodopsin [5–10]. An alternative, more generally applicable strategy exploits the observation that proteins are retained in the Golgi of mammalian cells in culture at 20˚C, allowing their release as a synchronous wave of secretion by raising the temperature [11]. Experiments using these approaches have identified multiple sorting signals for apical and basolateral cargoes and have revealed that there are a variety of trafficking routes to each membrane domain, some of which pass through intermediate endosomal compartments [2,12,13]. Nevertheless, it is still unclear how specific cargoes are targeted to the appropriate membrane domain and how this is controlled by the apical-basal polarity system [1].

Although these approaches have proved powerful, they involve non-physiological conditions or work only for specific cargoes. For example, the low temperature used to arrest secreted proteins in the Golgi can also affect other cellular processes, while the total block to the exit of proteins and lipids from the TGN might have knock-on effects on the localisation of essential trafficking factors. These limitations have been overcome by the development of the Retention using Selective Hooks (RUSH) technique [14]. In this approach, the labelled cargo is fused to the Streptavidin-binding peptide (SBP), and the hook is provided by

Streptavidin fused to KDEL, the ER retention signal (Figure 1A). The binding of SBP to Streptavidin-KDEL retains the cargo in the ER, until the addition of biotin triggers its release by binding with high affinity to Streptavidin and displacing the SBP-tagged cargo, which continues along the secretory pathway.

Most studies of secretion in epithelia have been performed in a small number of immortalised mammalian cell lines, such as Madin-Darby canine kidney (MDCK) cells, which are derived from the kidney tubule epithelium. We therefore set out to exploit RUSH to investigate how secretion is targeted to the apical and basolateral domains in a more typical secretory epithelium that is amenable to genetic analysis, using the *Drosophila* follicular epithelium as a model [15]. The follicle cells surround developing germline cysts, and the epithelium therefore adopts an elongated spherical shape with an external basal domain, which facilitates imaging along the apical-basal axis but has the disadvantage that the apical surface lies up to 10μm above the coverslip. In contrast to mammals, the Golgi is dispersed in insects [16]. Upon release from the ER, a fluorescent cargo traffics to multiple Golgi mini-stacks per cell, each of which acts as a source of post-Golgi carriers that translocate to the plasma membrane. The dispersed Golgi mini-stacks contain more fluorescent cargo than the post-Golgi carriers that bud from them, and tracking the movements of these vesicles is therefore challenging because of the crowded cellular environment and a low signal to noise ratio (SNR). To address these problems, we report here the development of a machine learning based approach to improve the accuracy and efficiency of vesicle tracking.

Many different tracking algorithms have been developed in recent years [17–25].
One major advance has come from the development of deep learning (DL) methods, which have become the standard solution for a wide range of image analysis tasks, including segmentation, detection, registration, and more recently object tracking. For example, DL approaches can enhance target detection, which improves the tracking of objects with complex shapes and facilitates frame-to-frame linking [19,26–32]. However, these machine learning methods usually require an extensive training dataset that must be updated for each new experimental system, which can be impractical and time consuming. Some of these existing tools were also developed for particular imaging techniques, while others perform poorly in a noisy environment.

To address these drawbacks, we have developed an MSP (Multi-Scale Particle) framework to facilitate particle tracking in a noisy environment. In this approach, vesicle detection is supported through a compact 2-layer convolutional neural network (CNN) that enables fast candidate selection and requires very little training data. In separate steps, the detected vesicles in consecutive frames are linked into short tracklets and these tracklets are then joined into longer tracks. A dedicated viewer allows the user to interact with the tracking algorithm at each step to optimise parameters and curate the outputs, and provides tools to measure, characterise and display the extracted trajectories. This tracking software is therefore distinct from other more automated approaches that require much larger training datasets. This software outperforms other similar software packages and has enabled us to determine the trajectories of apical and basolateral cargoes in the follicle cells in wild-type and mutant conditions. This has revealed the central of microtubules in determining where apical cargoes are secreted. In addition, our analysis shows that different ECM cargoes traffic to opposite sides of the basal region of the lateral domain, demonstrating that epithelial cells have the capacity to perform bidirectional, planar polarised secretion.

Results

Using RUSH to visualise polarised secretion

To examine apical secretion using RUSH in the *Drosophila* follicle cells, we inserted SBP and the HaloTag self-labelling tag after the signal peptide of Cadherin 99c (Cad99c) under the control of the GAL4 system (Figure 1B). Cadherin 99c is the *Drosophila* orthologue of the human Usher cadherin PCDH15 and is expressed in the follicle cells throughout oogenesis, where it localises to the apical microvilli [33,34]. For the basolateral cargo, we chose SNAP-tag labelled Nidogen, as it is a monomeric extracellular matrix protein that localises to the basement membrane beneath the follicle cells and is presumably secreted from the bottom third of the lateral membrane like Collagen IV [35–38].

When SBP-Halo-Cad99C is expressed in the follicle cells under the control of traffic jam-Gal4 in the absence of the Streptavidin-KDEL hook and labelled with cell-permeable fluorescent HaloTag ligand, it localises to the apical domain, although some protein leaks into the lateral

domain because of over-expression (Figure 1C). Similarly, SBP-SNAP-Nidogen localises to the basement membrane like the endogenous protein, demonstrating that both constructs contain functional trafficking signals (data not shown). Expressing two copies of UAS-Streptavidin-KDEL is sufficient to retain all SBP-Halo-Cad99C in the ER without activating the ER stress response, as monitored by the levels of BiP [39] (Figure S1). On the addition of biotin, it is released and most Cad99c is localised in the Golgi after 15 minutes (Figure 1C), partially co-localising with the trans-Golgi marker, Golgin 245 [40]. However, some Cad99c has already reached the apical plasma membrane after 10-15 minutes, and by 30 minutes, almost all labelled protein is localised to the apical microvilli, indicating that it rapidly transits the secretory pathway. Cad99c co-localises with Rab11 in puncta immediately below the apical membrane before it reaches the apical surface, indicating that it passes through the Rab11-positive recycling endosomes en route to the cell surface (Figure 1D)

To characterise the time course of Cad99c and Nidogen secretion, we made time-lapse movies of each labelled cargo after their release from the ER with biotin (Figure 2A, Movies S1&2). As seen in the fixed samples, most Cad99c localised to the Golgi after 10 minutes and to apical recycling endosomes after 20 minutes. Cad99c was detected on the apical surface before 20 minutes and reached maximal levels after 30 minutes. The trafficking of Nidogen to the basal surface showed very similar dynamics. We quantified the dynamics of trafficking through the secretory pathway in more detail by marking ER exit sites, the cis Golgi and the trans Golgi and TGN with endogenously-tagged Sec16, GMAP-210 and Golgin 245 respectively [41–43]. We labelled the plasma membrane with CellMask™ and measured the co-localisation of Cad99c with each marker over time using the normalised Pearson correlation coefficient (Figure 2B and D, FigS2, Movies S3-6). Peak levels of Cad99C colocalised with ER exit sites at 11 minutes and with the trans-Golgi after 22-23 minutes, indicating that it takes about 11-12 minutes to exit the ER and traverse the Golgi cisternae. Cad99c first appeared at the plasma membrane after 11 minutes and the amount of apical protein increased approximately linearly over the subsequent 20 minutes. Cad99c accumulates at a similar rate at the TGN and at the plasma membrane with a time lag of 6-8 minutes, indicating that this is how long it takes to traffic protein from the TGN to the cell surface. Cad99c reaches the plasma membrane at a similar rate to that of Serpentine in the fly tracheal epithelium but is significantly faster than cargoes that have been tracked in

tissue culture cells using RUSH or VSVG-ts [6,14,44]. This may be because the follicle cells and trachea are intact secretory epithelia rather than transformed tissue culture cells and are therefore more efficient at polarised exocytosis.

We performed a similar analysis on the dynamics of Nidogen secretion, except that we used wheat germ agglutinin as a plasma membrane marker instead of Cell Mask, which does not efficiently label the basal plasma membrane (Figure 2C and E, Figure S2, Movies S7-10). This revealed that a significant proportion of Nidogen already localises to ER exit sites before release and that it reaches maximum levels in the trans-Golgi at 14 minutes, 8 minutes earlier than Cad99c. This may reflect the fact that Nidogen is a soluble cargo and can therefore concentrate in the ER lumen near the exit sites. Perhaps as a consequence, Nidogen starts to accumulate extracellularly slightly earlier than Cad99c.

The MSP-tracker and MSP-viewer programs

To examine the movement of post-Golgi carriers from the TGN to the plasma membrane, we performed fast time-lapse imaging of labelled cargoes 15-20 minutes after the addition of biotin, i.e. just after their peak accumulation in the TGN. This revealed that many Cad99c positive vesicles show processive movements towards the apical surface, whereas Nidogen-containing vesicles show more randomly-directed trajectories. However, tracking these movements was challenging due to the large number of small vesicles, their low signal to noise ratio compared to the much brighter Golgi and their dispersed origins from Golgi mini-stacks throughout the cytoplasm (Figure 3A). We therefore developed an automated tracking program, MSP-tracker, and a separate program, MSP-viewer, that allows users to review and analyse the extracted trajectories. Both modules have a graphical user interface (GUI) to make them straightforward to use.

MSP-tracker is an extended version of our particle tracking software that uses a convolutional neural network (CNN) for candidate vesicle selection and a two-step process to identify tracklets and then link them into trajectories [45]. The particle detection module consists of background subtraction step followed by the identification of spots of different sizes and brightness using a multi scale spot enhancing filter (MSSEF) [46] (Figure 3B). This first step creates a pool of candidate vesicles, but is rather noisy, as MSSEF cannot distinguish

between post-Golgi vesicles and Golgi ministacks or other background signals. A light-weight convolutional neural network (CNN) classifier then selects vesicles from the pool. The decreased number of parameters in the CNN compared to other approaches reduces the number of annotations required for training to a few hundred regions of interest (ROIs) and provides a fast candidate pruning process that significantly improves detection efficiency. The MSP-framework comes with a few networks that have already been trained, but the CNN classifier can be easily trained on new data if required. In the last step, the locations of the selected candidates are refined to provide sub-pixel localisation. Due to its computational efficiency, this step uses the iterative centre of-mass refinement [25]. This pruned and refined set of detected particles is then handed to the linking algorithms.

The detected particles in different frames are joined into tracks with a two-step linking approach. First, short tracks (tracklets) are formed based on the vesicles' proximity in time and space. These short tracklets are then linked based on their characteristics, in a process called track-linking. Given the complex and changeable behaviour of the particles, this multi-step approach builds trajectories without assumptions about the type of movement. The first step takes into account the distance between detections and existing tracks, solving the assignment problem sequentially for each frame. The problem can be described as minimum-weight matching and is solved with the Hungarian algorithm [47]. Detections that are not matched with any of the tracks start their own new track. The length of the track is limited, as well as the number of the sequentially missed frames. This way, short reliable tracks are formed based on the spatial and temporal distances.

Each tracklet can be described by its position in time and space, its speed and direction of movement and its appearance. A Bayesian network (BN) uses these characteristics to calculate a connectivity score for each pair of tracklets, which represents the probability that these tracklets are linked. The connectivity score is only calculated for tracklets that are close in space and time, as this significantly reduces computation time and increases the efficiency of the method. When all the possible tracklet pairs have been evaluated, the tracklets are assembled into tracks using the Hungarian algorithm [47]. The minimum number of points in the trajectory can be set manually by the user and it can be useful to filter by length to eliminate very short trajectories, which can arise from false

detections. MSP-tracker allows users to repeat the track-linking process with different settings to link tracks into larger trajectories, as a second pass can be beneficial in a dense environment or when some particles move much faster than the majority. In these cases, the first pass connects slow-moving particles (using a small value for the distance parameter) and the second pass connects faster moving ones (using a larger value for the distance parameter). The software displays the intermediate results from the vesicle detection and track-linking algorithms, revealing how parameter selection affects the output. The optimal parameters can then be saved in an external file for future reference. Finally, the extracted tracks are stored in a format compatible with MSP-viewer where the trajectories can be examined (Figure 3C).

MSP-viewer is the tool for exploring extracted tracks and allows the user to view the tracks, correct them if required, plot them and analyse their characteristics. The main window displays the image sequence overlaid with the plotted trajectories and a table of the individual trajectories (Figure 3C). The set of trajectories can then be filtered based on their duration (length), net or total distances travelled, mean curvilinear speed or trajectory orientation. The results can also be displayed as a circular plot of trajectory orientations based on track count or net distance travelled. Clicking on an individual track in the table opens a new window that shows the trajectory, a graph of the speed of vesicle movement over time and a table listing the net distance travelled, the mean curvilinear and straight line speeds over the whole trajectory and when the particle is moving, as well as the maximum curvilinear speed (Figure 3D-F). The code for both MSP-tracker and MSP-viewer and a detailed manual with step-by-step instructions for installation and parameter settings are available on github (https://github.com/MariiaVision/msp_tracker).

Evaluation of MSP-tracker performance

To evaluate the performance of MSP-tracker under controlled conditions, we used twelve image sequences of 100 frames of computer-generated data from the particle tracking challenge [20]. The scenario mimics real data of moving vesicles at three density levels (low, middle and high), and at four different signal-to-noise ratios (SNR) of Poisson noise (1, 2, 4 and 7) (Figure 4A). We compared the performance of MSP-tracker to the tracking methods that participated in the particle tracking challenge using the five

performance measures used in the original challenge paper (Figure 4B) [20]. Linking performance is quantified by the degree of matching between the ground truth and estimated tracks, expressed by the α and β measures, and by two Jaccard similarity coefficients, one for entire tracks, JSC_θ, and one for track points, JSC. The α measure does not take into account spurious tracks and ranges from 0 (worst) to 1 (best), while the β measure has a penalty for spurious tracks, and therefore ranges from 0 to α. Both Jaccard similarity coefficients range from 0 to 1. The particle localisation accuracy is evaluated by the root mean square error (RMSE) of matching points in the paired tracks. The lines in Figure 4A represent the values for MSP-tracker and the coloured areas show the range of scores reported in the original challenge paper [20].

The performance of MSP-tracker falls within the upper range of the published results of the particle tracking challenge for the α and β measures but gives lower results for high density samples in the Jaccard similarity coefficient for track points, JSC. This may reflect the fact that the convolutional neural network was not trained on this type of artificial data and was developed to detect the vesicles of interest against a background of other fluorescent objects in the cell, such as the Golgi. However, MSP-tracker performs extremely well for the Jaccard similarity coefficient for the entire tracks, JSC_θ. This highlights its ability to link detections into the correct tracks, even if the detections inside the tracks are not complete.

A more relevant test for MSP-tracker is to evaluate its performance on real data that has been manually tracked to determine the ground truth. We therefore analysed whether MSP-tracker correctly identified tracks in 12 video sequences containing a total of 391 annotated tracks. To examine the performance of the tracker under different conditions, we included movies taken using both Airyscan and spinning disk microscopes, four different RUSH cargoes and imaged along cross-sectional and planar views of the egg chamber. The ground truth data was manually annotated using the ImageJ multi point tool [48] and MSP-viewer, which provides a faster and more convenient platform for tracing vesicle trajectories. The annotated positions of the particles do not provide subpixel localisation unlike automated methods, and the RMSE measure is therefore not provided for the data evaluation.

The results from MSP-tracker were compared with the performances of the most recent version of Trackmate [23,32], which is widely used as an ImageJ plugin and SpotTracking [49], which scored in the top 3 in most categories of the particle tracking challenge[20]. In addition to the linking measures that have already been mentioned, α, β, JSC and JSC_θ, we used a novel measure ɣ, which represents the proportion of manually annotated tracks that were detected by the software. MSP-tracker produced significantly better results than the two other tracking programs in all metrics (Figure 4C). This is mainly due to the detection component of the tracker, where the candidate pruning improves detection and therefore boosts tracker performance. Nevertheless, all three programs detect some spurious tracks, which is reflected in the low β and JSC_θ scores. This is largely due to the nature of the data itself. The dispersed mini-Golgi stacks can resemble vesicles, while some vesicles, located away from the focal plane appear as blurry and noisy areas that are challenging to detect. Given the uncertainty about how many of these "false positive" tracks are genuine, ɣ represents a more meaningful performance metric, since it measures the proportion of verified tracks that each software detected. MSP-tracker performed much better than the other programs on this metric, as it detected nearly 90% of the annotated tracks compared to 40% for Trackmate and SpotTracking (Figure 4C).

A key part of our analysis pipeline is to use MSP-viewer to manually curate the tracks after the automated track detection by MSP-tracker. MSP-viewer provides a straightforward and efficient platform to do this, resulting in a final track list that is as close to the ground truth as possible.

Tracking Cadherin 99c and Nidogen vesicles

We used automated tracking with manual curation to analyse the direction of Cad99c-positive vesicles movements at different stages of oogenesis and at different time points after the addition of biotin. At stage 8 when the follicle cells are still cuboidal, Cad99c-positive vesicles move in all directions. To quantify this, we counted the number of apically-directed tracks (defined as tracks whose orientation fell within 45˚of apical), compared to lateral (left and right 90˚ quadrants) and basal. 31% of vesicles moved apically, 52% moved laterally and 17% basally (Figure 5A, Table S1, Movie S11). The apical tracks are longer than the basal ones, however, and this results in a mean apical displacement per track of 0.49 μm ±0.26 (s.e.m), which is sufficient to deliver Cad99c to the apical plasma membrane (Figure

5D). The columnar follicle cells at stage 9 show a much stronger directional bias towards the apical surface, with 73% of the Cad99c-positive vesicles moving apically compared to 17% basally, giving a mean apical displacement per track of 1.32 μm ± 0.18 (s.e.m) (Figure 5B,D, Movie S12). This increase in directionality correlates with the more highly polarised organisation of the microtubules along the apical-basal axis of columnar follicle cells compared to the cuboidal cells at stage 8 (Fig S8G and K) [50–52]. The strong directional bias in the movement of Cad99c vesicles starts to diminish after 30 minutes post biotin addition, when most Cad99c has already reached the apical membrane, presumably because secretion is now balanced by endocytosis in the opposite direction (Figure 5C, Movie S13), indicating that MSP-tracker can also map the trajectories of endocytic vesicles. We saw the same trend when tracking vesicle movements imaged on a spinning disc microscope, with a strong apical bias in Cad99c tracks (Figure S5A, Movie S14) that is lost when imaging later after biotin addition (Figure S5B, Movie S15).

A similar analysis of the trajectories of Nidogen vesicles revealed that they move in more random directions with a slight bias towards the basal side (Figure 6A, Table S1, Movie S16). 33% of vesicles move towards the basal quadrant, compared to 25% apically and 41% laterally (Table S1). Nevertheless, the weak directional bias leads to a mean basal displacement per track of 0.17 μm ± 0.09 (s.e.m) (Figure 6B). Studies on the secretion of another ECM protein, Collagen IV, in the follicle cells indicate that it is secreted in a planar-polarised manner from the basal third of the lateral membrane and that it is transported there in Rab10^{+ve} vesicles by Kinesin and Khc73 [37,38]. During stages 3-8 of oogenesis, the follicle cells collectively migrate over the underlying basement membrane, causing the egg chamber to rotate around the anterior-posterior axis, in a process that aligns the collagen fibrils so that they form a molecular corset around the dorsal ventral axis [38,53]. Imaging of Rab10^{+ve} vesicles revealed that these move towards the trailing edges of the migrating cells, where Collagen IV is thought to be secreted [37,54]. We therefore examined whether Nidogen carriers also show planar-polarised movements basally by imaging horizontal planes of the epithelium either in the middle of the cell or just above the basal surface (Figure 6C and D, Movies S17 and 18). The vesicle tracks showed little planar-polarised bias in their directions of movement in the middle of the cell, but showed a pronounced planar polarisation basally, with 45% moving towards the leading edge, compared to 30% towards the trailing

edge. Surprisingly, this is the opposite bias to that reported for Rab10^{+ve} vesicles, which are presumed to contain Viking (Collagen IV) [37] (Figure 6D). Movies collected on the spinning disc microscope showed the same bias (Figure S6, Movies S19-21).

To test whether Nidogen is transported to the leading edge in Rab10^{+ve} vesicles, we co-expressed YFP-Rab10 with the Nidogen RUSH construct. Rab10 co-localises with Nidogen in large vesicular compartments at the base of the cells and remains associated with Nidogen vesicles after they leave this structure (Figure 7A and B, Movie S22). Fast imaging of the basal side of the cells 15 minutes after the release of Nidogen with biotin revealed that >75% of moving Nidogen-containing vesicles were also Rab10^{+ve} (Figure 7C; Movie S23). Indeed, tracking Rab10^{+ve} vesicles in these movies revealed a similar directional bias to Nidogen vesicles, with 45% moving towards the leading edge (Figure 7D-E, Table S1, Movie S24-25). This is the opposite bias to that observed by Zajac and Horne-Badovinac (2022) in cells that did not over-express Nidogen. We therefore tracked Rab10^{+ve} vesicles in cells without UAS-Nidogen and observed a bias towards the trailing edge (Figure 7F, Movie S26). Thus, releasing a pulse of Nidogen through the secretory pathway shifts the direction of Rab10^{+ve} vesicle movement towards the leading edge.

Since these results suggest that follicle cells secrete Nidogen and Collagen IV from opposite sides of the basal region of the lateral surface, we set out to confirm that Collagen IV is secreted from the trailing edges of the cells. Since Collagen IV is a dimer, it was not possible to use RUSH to examine its movement within the cell. However, it accumulates laterally between cells, before being drawn into alignment in the basal ECM by attachment to the existing ECM and follicle cell rotation[38]. We therefore imaged egg chambers containing homozygous clones that lacked GFP-Collagen IV surrounded by cells expressing GFP-Collagen IV from the *viking* protein trap line. By labelling the extracellular Col IV in living egg chambers using a fluorescently-labelled anti-GFP nanobody, we could examine which side of the cell Col IV is secreted while observing the direction of rotation. As expected, more lateral GFP-Col IV could be detected at trailing edges that faced GFP-Col IV non-expressing cells than at the leading edges (Figure 7G). Thus, follicle cells transport Nidogen and Col IV in opposite directions along the basal array of microtubules to bias their secretion at the leading and trailing edges respectively.

The role of microtubules in Cadherin 99c and Nidogen transport

To test the ability of the MSP software to detect changes in the behaviour of post-Golgi carriers, we examined the effects on Cad99c trafficking of disrupting microtubule-based transport. In most epithelial cells, microtubules are nucleated from noncentrosomal microtubule organising centres at the apical cortex and form apical-basal arrays with their minus ends apical [51,55–57]. Cad99c carriers are thought to be transported along these microtubules by the minus end directed motor protein, Dynein [52]. We therefore used the MSP package to analyse Cad99c carrier movements in stage 8 and 9 follicle cells heterozygous for a dominant mutation in the Dynein heavy chain, *Dhc*$^{8-1}$, which reduces the speed of the dynein-dependent transport [58] (Figure 8A, Figure S8A, Movie S27&28). The net speed of apical movements at stage 9 was significantly reduced in the slow dynein mutant: in wildtype egg chambers, vesicles moved apically with a mean net speed of 1.1 µm/sec ± 0.34 (sd), whereas basally-directed vesicles moved more slowly at 0.85 µm/sec ± 0.19 (sd). In the *Dhc*$^{8-1}$/+ mutant, however, the apically-directed vesicles moved at the same speed as the basally-directed vesicles (0.85 µm/sec ±0.34 (sd) and 0.83 µm/sec ±0.22 (sd) respectively), which were unaffected by the mutation (Figure 8D). This observation confirms that Dynein is the major motor that transports Cad99C vesicles to the apical surface, whereas another slower motor mediates the basal movements. *Dhc*$^{8-1}$/+ follicle cells also showed a loss of the apical bias in the direction of vesicle movement, with equal numbers of tracks extending basally and apically in stage 9 egg chambers (Table S1). This correlates with a 40% reduction in the frequency of Cad99C vesicle movements, suggesting that the mutant Dynein is less active than the wild-type motor. As a consequence, the mean displacement per track is altered to 0.1 µm ±0.23 (s.e.m.) basally in stage 8 egg chambers, and 0.07 µm ± 0.3 (s.e.m) basally in stage 9 egg chambers, indicating that Cad99c is not translocated apically (Figure 8E). Consistent with this, Cad99C was secreted only laterally at stage 8 in 15.8% of movies of *Dhc*$^{8-1}$/+ mutant cells and a further 26.3% showed secretion at the lateral membrane before the apical membrane (Figure 8F).

Colcemid treatment leads to the depolymerisation of almost all microtubules in the follicle cells, but a few stable microtubules persist in the apical region of the cells (Figure S8). This leads to a dramatic reduction in the number of Cad99c vesicle movements,

indicating that most Cad99c trafficking is microtubule-dependent (Figure 8B, Figure S8B, Movies S29 and S30). Depolymerising microtubules with colcemid had an even more dramatic effect on where Cad99C is secreted, with 71% of movies showing only lateral secretion or secretion laterally before apically (Figure 8G). This indicates that dynein-dependent apical transport along microtubules is the primary determinant of where Cad99c is secreted and that implies that Cad99c-containing vesicles are competent to fuse with the lateral membrane. During the final stages of its secretion, Cad99C normally accumulates in Rab11^{+ve} recycling endosomes beneath the apical membrane (Figure 1D) and is then transported to the membrane by Myosin V [52]. Colcemid treatment leads to the partial relocalisation of the Rab11^{+ve} endosomes to the lateral side of the cell (Figure S8D).

In contrast to Cad99c, the movements of Nidogen-containing vesicles were unaffected by the *Dhc*$^{8-1}$ mutant, suggesting that their trafficking does not require Dynein (Figure 8D and I-J, Movie S31). Apically-directed Nidogen-containing vesicles move at the same speed as basally-directed ones in both wild-type cells and *Dhc*$^{8-1}$ mutant cells (Figure 8D). Furthermore, both move much faster than Cad99C vesicles, with an average speed of 1.5 μm/sec ± 0.4 (sd) apically and 1.4 μm/sec ±0.3 (sd) basally. This is significantly faster than kinesin or dynein, suggesting that the basal transport is mediated by Khc73, which transports Collagen IV basally and is a member of the KIF3 family of super-processive, fast plus end-directed motors [37,59,60]. Since almost all microtubules grow from the apical surface with their plus ends extending basally, Khc73 can transport Nidogen vesicles basally, but is unlikely to be responsible for their fast apical movements. By contrast, the planar polarised movements of Nidogen vesicles along the basal surface are significantly slower, with a mean speed of 0.7 μm/sec, in agreement with the proposal by Zajac et al. (2022) that Kinesin is the predominant motor that transports vesicles along basal microtubules. Consistent with the requirement for Kinesin and Khc73 for Nidogen vesicle transport, depolymerising microtubules with colcemid blocked Nidogen secretion (Figure 8H). Indeed, most Nidogen appeared to remain in the Golgi, as shown by its co-localisation with Golgin245, suggesting that the exit of Nidogen from the TGN requires the pulling forces exerted by microtubule motor proteins. Finally, the basal movements of Nidogen vesicles in both directions were significantly faster in *Dhc*$^{8-1}$ mutant cells, although the bias in the direction of Ndg tracks was not affected (Figure 8D and K-L, Movie S32). This suggests that transport towards both

the leading and trailing edges is mediated by plus end directed motors that are antagonised by dynein. Furthermore, vesicle movements towards the leading edge are significantly faster than those towards the trailing edge in *Dhc*$^{8-1}$/+, suggesting that different motors move the vesicles in each direction.

Discussion

Here we report the development of a new program, MSP-tracker, which uses a convolutional neural network (CNN) to automatically detect the trajectories of vesicles or particles moving in the cytoplasm. The program first uses classical methods to detect spots or particles and then uses a CNN to select the vesicles or particles from this pool of candidates. This approach means that the CNN only requires small training sets and the same trained model can be used to analyse multiple experiments if the vesicles are similar in size and appearance. This approach is particularly good at tracking vesicle movements in noisy environments where other organelles are also visible in the same channel, such as the mini-Golgi stacks in our RUSH experiments. The user-friendly interface of MSP-tracker also allows the results to be monitored at each step of the algorithm, facilitating the selection of the optimal parameters for vesicle selection and track linking.

We tested the performance of MSP-tracker using both the particle tracking challenge [20] and a selection of real data of movies of moving vesicles containing secretory cargoes after their release from the endoplasmic reticulum. MSP-tracker did particularly well with the real data, correctly classifying 90% of the ground truth vesicle trajectories identified by manual annotation. Two other leading tracking algorithms identified less than half of these ground truth trajectories, demonstrating that MSP-tracker is significantly better at analysing vesicle movements in a noisy environment.

The companion program, MSP-viewer is an essential part of the software, as it allows users to review and correct the tracking results before analysing the extracted trajectories.

This feature significantly improves the resulting data, as it allows users to delete spurious trajectories, which are usually short and can be removed simply by filtering by length. In addition, one can add any trajectories that were missed by MSP-tracker, which are most often tracks that were not linked correctly. Once this straightforward manual curation is complete, MSP-viewer can then be used to analyse the speeds and directions of the resulting trajectories, providing detailed information on the dynamics of vesicle movement. Both MSP-programs are available at https://github.com/MariiaVision/msp_tracker and the software can be run on Windows, MacOS or Unix machines, or remotely on a high performance computer, when analysing large video sequences that require longer computation times. One can also import tracks from other algorithms into MSP-viewer and use the simple, but powerful, interface to curate the tracks.

To demonstrate the utility of the MSP software, we analysed the trafficking of Cad99C to the apical surface of the follicle cells, as this has been shown to depend on Dynein and the apical-basal microtubules in studies in fixed samples [52]. Consistent with these results, we observe that Cad99c vesicles predominantly move towards the apical surface, particularly at stage 9, and that these movements are microtubule-dependent, as they largely cease after treatment with colcemid. Analysis of the vesicle trajectories reveals that they move faster and further towards the apical surface than they do basally, suggesting that different motors mediate their movements in each direction. Furthermore, a slow Dynein mutant reduces the speed of apical movements without affecting the basal ones. These results demonstrate that Dynein directly transports Cad99c vesicles towards the apical surface, rather than playing an indirect role, whereas another slower motor mediates the basal movements.

Both the slow Dynein mutant and colcemid treatment lead to the secretion of Cad99c at the lateral membrane of the follicle cells, indicating that the apical-basal organisation of the microtubule cytoskeleton is the main determinant of where different cargoes are secreted. This observation is surprising since the fusion of vesicles containing apical cargoes with the apical membrane requires a specific t-SNARE protein in mammalian cells, Syntaxin 3, whereas the fusion of basolateral cargo vesicles requires a different t-SNARE, Syntaxin 4 [61,62]. *Drosophila* lacks clear homologues of Syntaxin 3 and 4, and it is therefore possible that

the apical and basolateral membranes contain the same fusion machinery, so that vesicles with apical cargoes are competent to fuse with the basolateral membrane and vice versa. In this case, the site of Cad99c secretion would be solely determined by its Dynein-dependent transport to microtubule minus ends at the apical membrane, explaining why it is mistargeted laterally when Dynein and microtubules are disrupted. Similarly, the secretion of Collagen IV at the basal part of the lateral membrane depends on its basal transport by Khc73 and Kinesin, with knockdown of both motors leading to its secretion at the apical region of the lateral domain [37]. However, it is also possible that the mis-targeting of secretory cargoes is an indirect effect of disrupting microtubule-based transport, as t-SNARES also need to be delivered to the correct membrane. Microtubule disruption causes the mis-localisation of Syntaxin 3 to the basolateral domain of MDCK cells, inducing the secretion of apical cargoes basolaterally [63]. Thus, there may be specific apical fusion factors in *Drosophila* whose localisation also depends on Dynein and microtubules, and which lead to the lateral secretion of Cad99c when mislocalised, but the nature of these factors is unknown.

Knockdown studies have indicated that Khc73 is the main motor that transports ECM cargoes vesicles basally, while Kinesin may play a larger role in the planar polarised transport along the basal side of the cell [37]. Our results support this idea, since we observe that the Nidogen-containing vesicles move towards the basal side at 1.4 μm/sec, consistent with transport by the fast Kinesin 3 family member, Khc73, whereas the planar polarised movements across the basal surface occur at half this speed, as expected for Kinesin 1. Nidogen vesicles show a clear bias in their planar-polarised basal movements towards the leading edge of the migrating follicle cells, suggesting that Nidogen is mainly secreted on this side of the cell. This is the opposite side from where most Collagen IV is secreted, as inferred from the trafficking of Rab10^{+ve} vesicles and the accumulation of Viking-GFP at the trailing edge of cells that abut non-expressing cells [37,54]. The membrane proteins that guide the follicle cell migration are also planar-polarsised, with Semaphorin 5c and Lar localising to the leading edges of cells, and Fat2 and Plexin A to the trailing edges [64–66]. Thus, the follicle cells have mechanisms to target the secretion of specific proteins to opposite sides of the basal surface. Epithelial cells are generally thought to traffic secreted proteins to either the

apical or basolateral plasma membrane, but the behaviour of Nidogen and Collagen IV demonstrates that they can target cargoes much more precisely.

Understanding how secretory cargoes are secreted to the correct domain of the plasma membrane requires being able to track and analyse vesicle movements at scale in a reliable and reproducible manner. Our results demonstrate that MSP-tracker in combination with the RUSH system provide a powerful approach to visualise the complex trafficking of secretory cargoes in epithelial cells. Combining these approaches with mutations and drugs that disrupt motors and trafficking factors may reveal the underlying logic of polarised secretion in epithelia.

Acknowledgments

We thank Akira Nakamura for providing us with the Rab11 antibody, the Bloomington and Kyoto Stock centres for fly lines, Franck Perez for introducing us to the RUSH system and the St Johnston lab for help and advice. We would like to acknowledge the Gurdon Institute Imaging Facility for help with microscopy and image analysis. This work was supported by a Wellcome Trust Collaborative award (203285), a Wellcome Principal Fellowship to DStJ (080007, 207496), a BBSRC project grant (BB/P026486/1) and by centre grant support from the Wellcome Trust (092096, 203144) and Cancer Research UK (A14492, A24823). JR is an adjunct Professor at the Ludwig Institute for Cancer Research, University of Oxford. Work in SL's laboratory was supported by the Deutsche Forschungsgemeinschaft (SFB 1348 "Dynamic Cellular Interfaces"; SFB 1009 "Breaking Barriers"), the "Cells-in-Motion" Cluster of Excellence (EXC 1003-CiM), and the University of Münster.

Materials & Methods

Imaging systems

Two microscopes were used to collect the RUSH tracking data for this study, a Zeiss 880 Airyscan microscope using the Airyscan "Fast" mode, using the 63x Water objective 1.2 NA, and a custom built spinning disk microscope (Sirinakis et al., 2022).
The UAS-Rab10-YFP tracking data were collected on the Zeiss 880 Airyscan using Airyscan "Fast" mode with the 63x oil immersion objective 1.4 NA.
All other images were obtained using a Leica SP8 with white light laser, using the 63x oil objective, 1.4 NA.
For information on acquisition speeds for the tracking movies, microscope system used, Halo/SNAP dye used, and other parameters see figure legends.

Fly Husbandry and lines

Fly lines used in this study are described in **Table 2**.
For RUSH experiments flies were raised at 25˚C until pupation, at which point they were moved to 18˚C to reduce leakiness of the RUSH system.

Flies heterozygous for *Dhc64c*$^{8-1}$ show reduced trafficking speeds of *bicoid* mRNA particles [58], and we therefore used this mutant to test if the speeds of Cad99c and Ndg vesicles movements were affected by this allele.
UAST-SBP-Halo-Cad99c was created by cloning the signal peptide of the Cad99c followed by a GSGSGSG linker, the sequence for streptavidin binding peptide (SBP), PAG, then the HaloTag sequence, another GSGSGSG linker, and the rest of Cad99c into pUAST(AttB) using NEB HiFi assembly. UAST-SBP-SNAP-Ndg was created by cloning the signal peptide of cg25c followed by the SBP sequence, then a Pro-Ala-Gly linker, then the SNAP sequence, a GSHMRSRPTS linker and the Ndg sequence into pUAST(AttB) using NEB HiFi assembly. The cargoes were designed to ensure that the SBP was facing the lumen of the ER and therefore could access the streptavidin-KDEL hook. Transgenic flies made by injecting into the listed landing sites.

Sec16 was endogenously tagged using CRISPR/Cas-mediated homology-directed repair [67,68]. A pCFD3-gRNA-Sec16 plasmid and a donor construct were injected together into TH_attP2 embryos at a concentration of 75ng/µl and 100ng/µl, respectively. To make the donor

construct, EGFP along with a GSGSGSG linker and ~1000bp long homology arms were cloned into pBluescriptSK+ using NEB HiFi Assembly. The endogenous Sec16 ATG was removed, and to prevent Cas9 from re-cutting the repaired DNA ,the PAM site was mutated. Injected flies and their progeny were screened for the presence of the GFP sequence and multiple independent stable lines were recovered.

Table 2 – Fly lines used in this study

Line		Location	Reference	Notes
1	2xUAST-SA-KDEL/CyO	attP40 and attP51C1	[44]	
2	UAST-SBP-Halo-Cad99c	attP2	This Study	
3	UAST-SBP-SNAP-Ndg	attP2	This Study	
4	TrafficJam-Gal4/CyO (P{GawB}NP1624)	2L	[69]	
5	GFP-Sec16	Endogenous locus (X)	This Study	
6	GFP-Golgin-245	Endogenous locus (2R)	[70]	
7	GFP-GMAP (Gmap^{CC00492})	Protein trap (X)	[71]	
8	w;; Dhc64c$^{8-1}$/TM6B	3L	[72]	
8	w; 2xUAST-SA-KDEL/CyO; UAST-SBP-Halo-Cad99c/TM6B			Combination of 1 & 2
9	w; 2xUAST-SA-KDEL/CyO; UAST-SBP-SNAP-Ndg/TM6B			Combination of 1 & 3
10	GFP-Sec16; TrafficJam-Gal4/CyO			Combination of 4 & 5
11	w; TrafficJamGal4, GFP-Golgin245/CyO			Recombination of 4 & 6

12	GFP-GMAP; TrafficJam-Gal4/CyO			Combination of 4 & 7
13	w; TrafficJam-Gal4/CyO; Dhc64c[8-1]/TM6B			Combination of 4 & 8
14	y, w; P{UASp-YFP-Rab10}21	3L	RRID:BDSC_9789	
15	y1 w*; P{PTT-un}vkgG00454, FRT40A / CyO	2L	RRID:BDSC_98343 recombined with FRT 40A	Recombination of Vgk-GFP trap line and FRT40A
16	hsFlp; P{w[+mC]=Ubi-mRFP.nls}2L P{ry[+t7.2]=neoFRT}40A/CyO	2L	hsFlp added to RRID:BDSC_34500	

Sample preparation for live imaging

Flies were fattened on yeast for 2 days at 18˚ C. Ovarioles were dissected out of ovaries and the muscle sheath in Schneider's insect medium supplemented with insulin (7.5 µg/ml, Merck I9278). For SNAP-Ndg flies, ovarioles were initially labelled in Schneider's plus 0.5 µM SNAP-SurfaceBlock for 5-10 min to block non-egg-chamber-autonomous Ndg labelling of the ECM. Ovarioles were labelled in Schneider's plus 1 µM SNAP or HaloTag ligands for 15-20 minutes at room temperature before being transferred to an 8-well poly-lysine coated µ-slide (Ibidi) in 100 µl Schneider's medium. To induce release of the cargo from the ER, 100 µl Schneider's containing 800 µM D-Biotin (Merck) was added to the medium, to give a final concentration of 400 µM D-Biotin.

For colcemid treated ovarioles the abdomens of flies were injected with 0.4 mg/ml colcemid in Schneider's medium 1 hour before dissection. Labelling and cargo release were carried out as above, but 0.4 mg/ml colcemid was present in all the solutions. Colcemid stocks were dissolved in DMSO, as the usual carrier ethanol caused independent effects on the egg chambers, while DMSO did not.

Correlation analysis for cargoes with CellMask, GFP-Sec16, and GFP-Golgin245

Image analysis was carried out using Fiji [48]. iPearson's correlation coefficient was calculated for the cargo and marker (e.g. Cell Mask, GFP-Sec16, GFP-GMAP, GFP-G245) signal in each frame of the time series using a custom script (https://github.com/gurdon-institute/Egg_Chamber_Analysis/blob/main/Pearson_frames.py).

For Cell Mask, GFP-GMAP, GFP-G245, and UAS-Rab10-YFP, the zero timepoint was set to a value of zero, and the difference between other timepoints and the zero timepoint was calculated for each movie. For GFP-Sec16, as there is significant overlap at the zero timepoint, we set the endpoint of the movie to a value of zero, and calculated the difference between the other timepoints and the endpoint for each movie.

The changes in correlation were then entered into GraphPad Prism, and each dataset transformed to be on a scale of 0-1 for graphing purposes. The transformation was Y=Y/K, where K=the mean maximum change in correlation. We were not able to use the raw correlation values, as the brightness of SNAP/Halo and CellMask labelling varies from egg chamber to egg chamber, whereas the change in correlation is consistent between samples.

Quantifying Nidogen secretion with WGA (Wheat Germ Agglutinin)

We were unable to use the Pearson's correlation for WGA as the staining changed both in brightness and localisation throughout the movie (i.e. in the beginning of the movie the basal surface of the egg chamber was labelled, but by the end it was brighter, and the lateral and apical membranes were also labelled)., We therefore quantified basal signal of Nidogen by using the basal WGA signal to define a basal region.
Egg chamber basal signal was quantified using a custom script (https://github.com/gurdon-institute/Egg_Chamber_Analysis/blob/main/Jenny_Basal_MeasureROICheck1_5basalR.py) to identify egg chambers and measure a 1.5 µm inner band containing the basal membranes of follicle cells. In order to robustly map egg chamber ROIs, the script first finds the largest WGA signal region in each frame, and then uses the convex hull if its area is greater than twice that of the original ROI. Egg chambers in each frame were then filtered to use the mapping from the previous frame if there is an overlap of less than 0.75. This gives reliable, roughly ellipsoid ROIs in frames where signal intensity varies, and a continuous boundary is not detected.

The output of the script includes a measurement of the mean brightness value in the Basal ROI. This was used to calculate the change in brightness over time, with time zero set to a value of zero. The values were then entered into GraphPad Prism, and each dataset was again transformed to be on a scale of 0-1 for graphing purposes. The transformation was Y=Y/K, where K=the mean maximum change in brightness.

Table 3 Number of movies used for cargo marker correlation analysis

Cargo →	**Cad99c**	**Ndg**
Marker ↓		
Sec16	10	11
GMAP	8	15
G245	11	12
CellMask	9	N/A
WGA	N/A	9
Rab10	N/A	16

Antibody stainings of RUSH egg chambers

For antibody stainings of egg chambers, ovaries of fattened flies were dissected into Schneider's medium supplemented with insulin. Ovarioles were incubated in Schneider's medium plus 400 µM biotin for 0, 15, or 30 minutes before being transferred to 4% formaldehyde in PBS and fixed for 20 minutes with rotation. Ovarioles were washed 3x5min in PBS, then incubated with Halo-TMR ligand (Promega) for 1 hour at 37˚C with shaking at 500rpm. Samples were washed 3x5 min in PBS then blocked in PBT (0.2% Tween20) with 10% BSA overnight at 4˚C. Ovarioles were then incubated for 48 hours at 4˚C in PBT 1% BSA with 1:2000 Rabbit anti-Rab11 [73] and 1:1000 Goat anti-Rabbit. Ovarioles were then washed 4x30min in PBT 1% BSA, then stained overnight at 4˚C with 1:500 Donkey anti-Rabbit Alexa488 and Donkey anti-Goat Alexa647 secondary antibodies in PBT 0.1% BSA. Samples were washed 3x10 min in PBT and mounted in Vectashield plus DAPI (Vectorlabs). Images were taken on the Leica SP8 WLL with the 63x oil objective. 1.4 NA.

Microtubule stainings of egg chambers.

For microtubule stainings of egg chambers, fattened flies were either mock injected with Schneider's medium, or with 0.4 mg/ml colcemid in Schneider's medium, 1 hour before dissection. Ovaries were dissected into either Schneider's medium supplemented with insulin, or also containing 0.4 mg/ml colcemid. Ovarioles were incubated for 30 minutes before being transferred to 10% formaldehyde in PBT (2% Tween20) and fixed for 10 minutes. Ovarioles were washed 3x5min in PBT (2% Tween20), then blocked in PBT (0.2% Tween20) with 10% BSA for 2 hours. Ovarioles were then incubated overnight at 4˚C in PBT (0.2% Tween20) 1% BSA and a 1:200 of FITC-conjugated anti-α-tubulin antibody (F2168, Merck, clone DM1A). Ovarioles were then washed 6x10min in PBT (0.2% Tween20) and mounted in Vectashield plus DAPI (Vectorlabs). Images were taken on the Leica SP8 WLL with the 63x oil objective. 1.4 NA.

Staining and quantification of extracellular Collagen IV at leading and trailing cell edges

hsFlp / + ; P{PTT-un}vkgG00454, FRT40A / nls-RFP, FRT40A females were collected and fattened on yeast (with males present), and subjected to 2-3 x 2hour 37˚C heatshock at 12 hour intervals. Alternatively pupae were heatshocked for 3 days with 2hour 37˚C heatshock at 12 hour intervals, and then adults fattened for 24-48 hours at 25˚C with yeast.

Ovaries were dissected out in Schneider's supplemented with insulin, and the ovarioles removed from the muscle sheath. Ovarioles were transferred to a drop of Schneider's with 1:50 dilution of Atto647n GFP-nanobody (Proteintech) to label the extracellular Collagen for 20 minutes. Ovarioles were transferred to fresh Schneider's and imaged as previously on an 8-well poly-lysine coated μ-slide (Ibidi). Timelapse Z-stacks were taken to allow the direction of rotation to be determined. The amount of extracellular collagen at the leading and trailing edges of the cells was then measured as follows. In FIJI [48] a segmented line was drawn along the leading or trailing edges of a patch of cells. This was converted to an area, the area expanded to a band of ~0.2um wide and the integrated density was measured. The

integrated density was divided by the number of cells in the patch and used to compare Collagen levels at the leading and trailing edges of the cells. Non boundary cells (i.e. those that contacted Vkg-GFP exprssing cells on both sides) were measured as a control.

Using MSP-tracker and MSP-viewer to track Cad99c, Ndg and Rab10 particles.

MSP-tracker was used to find particle tracks by following the method described in the user manual. MSP-viewer was used to assess the tracks found by MSP-tracker. Tracks were filtered by length to remove short (<700 nm) tracks. Remaining tracks were assessed on a track by track basis, and tracks were added manually, extended, edited, or deleted as necessary. Once tracks had been curated they were filtered to remove anything of less than 1000 nm long, and data were exported for further analysis. Excel was used to filter data into tracks going in different orientations, and Graphpad Prism was used to represent the data.

Western blotting

For each sample, three ovaries were homogenised in 25 µl Schneider's medium and 25 µl 2x Laemmli sample buffer and boiled at 95˚C. 10 µl of sample was loaded per lane on a 4-12% Bis-Tris polyacrylamide gel. The membrane was probed for BiP and Tubulin using rabbit anti-GRP78 (BiP) (StressMarq biosciences SPC-180S) at 1:1000, and mouse anti-tubulin (DM1A) at 1:1000. Secondaries used were goat anti-mouse Alexa 680 and goat anti-rabbit Alexa790 at a dilution of 1:10,000. The blot was imaged using a LiCor Odyssey system.

The tracking algorithm

The particle tracking algorithm of the MSP-framework consists of particle detection, and frame-to-frame object association (linking), Figure 2B. A pre-processing step enhances the appearance of the particles and improves the detection results. The background intensity is estimated from m consecutive frames (parameter can be set manually) and subtracted from the original frame. Finally, Contrast Limited Adaptive Histogram Equalization is applied to each frame to enhance the constrast.

The particle detection exploits an extended multiscale version of the spot enhancing filter (SEF). The SEF highlights spots by convolving the original image g(x, y) with a Laplacian-

of-Gaussian kernel LoG(x, y, σ). In the multi scale spot enhancing filter (MSSEF) [46], a set of SEF is applied sequentially with an intensity-based threshold after each iteration. This way, each iteration can be represented by Equation 1.

$$f(x, y, \sigma^k) = LoG(x, y, \sigma^k) * \left(b(x, y, \sigma^{k-1}) g(x, y)\right), \qquad (1)$$

where σ^k is a standard deviation of the LoG, and $b(x, y, \sigma^{k-1})$ is a binary mask extracted from the previous iteration. The threshold for each iteration T^k is defined by the mean intensity of the image μ^k and its standard deviation ς^k weighted by a user defined value c, Equation 2.

$$T^k = \mu^k + c\,\varsigma^k, \qquad (2)$$

The MSSEF exposes spots of different sizes and intensities and provides a reduction of the false detection rate related to the noise levels. The particle candidates are extracted based on the local maxima of the final MSSEF image. The coordinates of the candidates are used to define a region of interest (ROI) for each candidate. The default ROI size is 16x16 pixels, but the value can be adjusted for larger particle sizes. The CNN network classifies the ROIs to provide the final detection results. Training on small ROIs instead of an entire image allows one to use a light-weight CNN and apply the same learned model for imaging modalities provided that the appearance and size of the particles are similar.

The light-weight CNN architecture consists of two convolutional layers followed by max pooling and two fully-connected layers. The softmax activation function is used for the output layer, and Relu activation for the rest. The network is trained with binary cross-entropy loss function and root mean square propagation optimiser. The training data is augmented with rotation and flipping.

FInally, the locations of the selected candidates are refined to provide sub-pixel localisation using the iterative centre-of-mass refinement for the task [25].

The data association of the detected particles is solved with a two-step linking approach. The first step of the data association considers the distance between detections and existing tracks, solving the assignment problem sequentially for each frame with the Hungarian algorithm [47]. The weight is represented by the Euclidean distance between the

detection and already existing tracks. The formed tracklets are used to build longer trajectories.

A Bayesian network (BN) is used to compute the connectivity score for each pair of the tracklets. The score expresses the probability of these tracklets being linked based on their characteristics. Each variable (node) of the BN represents a single characteristic of the tracklet pair. These characteristics can be divided into four main groups: particle appearance, motion, location, and temporal position.

The particle appearance is represented by the intensity node. It indicates the similarity in average intensity between the ROIs in the last frame of the first tracklet and the first frame of the second tracklet. We expect the intensity of the particle to change along the trajectory but have similar values in succeeding frames. The motion is defined by two nodes: orientation and speed, where the similarity in orientation and speed of particle movement is defined. The location of the tracklets is defined based on the Euclidean distance between the coordinates of the last detection in the first tracklet and the first detection in the second tracklet. The temporal position is defined by sequence and gap variables. The sequence node characterises the successiveness of the first and second tracklets. This node is defined by two parent nodes: an order and an overlap. The gap node represents a temporal gap between the last detection in the first tracklet and the first detection in the second tracklet. The conditional probability table defines the contribution of each parent node. The introduced connectivity score is a binary variable with True meaning that the pair of tracklets are connected and belong to the same trajectory. The inference over the BN provides the probability of the connectivity score (CS) to be True, P_c:

$$Pc = P\left(CS = True \middle| I, O_r, S_p, O_d, O_v, G\right), \quad (3)$$

where I is a difference in intensities, O_r – in orientation, S_p- in speed, O_d – order of the tracklets, O_v – presence of the overlap and G is a temporal gap between the tracklets. When all the possible tracklet pairs are evaluated, the assignment problem is addressed with the Hungarian algorithm [47], and the tracklets are assembled into the tracks.

Parameters for detection and linking can be set in MSP-tracker GUI before running the tracking algorithm for the entire timelapse sequence.

Trajectory evaluation in track-viewer

The individual trajectory window of the MSP-viewer provides several quantitative trajectory measures, Table 3. Travelled distance is described by the total, net and maximum distances. The total distance is the entire trajectory length. In contrast, net distance represents the length between the first and the last points, and the maximum distance is defined by the largest interval between any two points of the trajectory. The total trajectory time is the number of frames scaled by the frame rate. The net orientation is defined by the first and last trajectory's points. The curvilinear speed is calculated from the total distance and can be defined as the mean of the instantaneous speeds, while the net distance defines the straight-line speed.

Table 3. Quantitative trajectory measures provided by the MSP-viewer

Measures	Formulation
Total distance travelled	$d_{total} = \Sigma_{i=1}^{N-1} d(p_i + p_{p+1})$
Net distance travelled	$d_{net} = d(p_i + p_N)$
Maximum distance travelled	$d_{max} = \max_i(d(p_1 + p_i))$
Total trajectory time	$t_{traj} = (N-1)t$
Net orientation	α
Mean brightness (normalised)	$b = \frac{1}{b_{max}N} \Sigma_{p=1}^{M} b_p$
Mean curvilinear speed	$v = \frac{1}{N-1} \Sigma_{i=1}^{N-1} \frac{d(p_i + p_{i+1})}{t}$
Mean straight-line speed	$v_{line} = \frac{d_{net}}{t_{traj}}$
Max curvilinear speed over a segment	$\max(v_1, v_2, \dots v_w)$
Number of moving segments	k
Average moving segment time	$t_{avg} = \frac{\Sigma_{j=1}^{k} t_j}{k}$
p_i - position of the ith particle; N – number of detections in the trajectory; t – trajectory time; M- number of pixels in the region of interest; b_p- pixel brightness; b_{max}- value of the brightest pixel in the image sequence	

The speed is evaluated for the entire trajectory (average speed), for the trajectory segments where the particle is moving (moving speed), and the maximum curvilinear speed is calculated for a given time interval by a sliding window over the moving segments. To allow segmentation of short trajectories, where the traditional Mean Square Displacement (MSD) methods are not applicable, we exploit a 1D U-Net segmentation [74]. The method provides segmentation of the directed motion of the particle from the remaining trajectory. The software provides both options, MSD and 1D U-Net based approaches.

Registration of the image sequence

Some image sequences have an undesirable movement of the egg chamber in the frame. We have registered the sequences before using the tracking software to prevent the movement's influence on the trajectory evaluation. We have used our custom Python code and the SimpleITK library [75], using mutual information between two neighbouring frames to register image sequences.

References:

1. Buckley, C.E., and StJohnston, D. (2022). Apical–basal polarity and the control of epithelial form and function. Nat Rev Mol Cell Bio, 1–19. 10.1038/s41580-022-00465-y.

2. Rodriguez-Boulan, E., and Macara, I.G. (2014). Organization and execution of the epithelial polarity programme. Nature reviews Molecular cell biology *15*, 225–242. 10.1038/nrm3775.

3. Mellman, I., and Nelson, W.J. (2008). Coordinated protein sorting, targeting and distribution in polarized cells. Nature reviews Molecular cell biology *9*, 833–845. 10.1038/nrm2525.

4. Tanos, B., and Rodriguez-Boulan, E. (2008). The epithelial polarity program: machineries involved and their hijacking by cancer. Oncogene *27*, 6939–6957. 10.1038/onc.2008.345.

5. Bergmann, J.E. (1989). Chapter 4 Using Temperature-Sensitive Mutants of VSV to Study Membrane Protein Biogenesis. Methods Cell Biol *32*, 85–110. 10.1016/s0091-679x(08)61168-1.

6. Hirschberg, K., Miller, C.M., Ellenberg, J., Presley, J.F., Siggia, E.D., Phair, R.D., and Lippincott-Schwartz, J. (1998). Kinetic Analysis of Secretory Protein Traffic and Characterization of Golgi to Plasma Membrane Transport Intermediates in Living Cells. J Cell Biology *143*, 1485–1503. 10.1083/jcb.143.6.1485.

7. Satoh, A., Tokunaga, F., Kawamura, S., and Ozaki, K. (1997). In situ inhibition of vesicle transport and protein processing in the dominant negative Rab1 mutant of Drosophila. J Cell Sci *110*, 2943–2953. 10.1242/jcs.110.23.2943.

8. Li, B.X., Satoh, A.K., and Ready, D.F. (2007). Myosin V, Rab11, and dRip11 direct apical secretion and cellular morphogenesis in developing Drosophila photoreceptors. J. Cell Biol. *177*, 659–669. 10.1083/jcb.200610157.

9. Satoh, A.K., O'Tousa, J.E., Ozaki, K., and Ready, D.F. (2005). Rab11 mediates post-Golgi trafficking of rhodopsin to the photosensitive apical membrane of Drosophila photoreceptors. Development (Cambridge, England) *132*, 1487–1497. 10.1242/dev.01704.

10. Iwanami, N., Nakamura, Y., Satoh, T., Liu, Z., and Satoh, A.K. (2016). Rab6 Is Required for Multiple Apical Transport Pathways but Not the Basolateral Transport Pathway in Drosophila Photoreceptors. PLoS Genetics *12*, e1005828. 10.1371/journal.pgen.1005828.

11. Matlin, K.S., and Simons, K. (1983). Reduced temperature prevents transfer of a membrane glycoprotein to the cell surface but does not prevent terminal glycosylation. Cell *34*, 233–243. 10.1016/0092-8674(83)90154-x.

12. Cao, X., Surma, M.A., and Simons, K. (2012). Polarized sorting and trafficking in epithelial cells. Cell Res *22*, 793–805. 10.1038/cr.2012.64.

13. Apodaca, G., Gallo, L.I., and Bryant, D.M. (2012). Role of membrane traffic in the generation of epithelial cell asymmetry. Nat. Cell Biol. *14*, 1235–1243. 10.1038/ncb2635.

14. Boncompain, G., Divoux, S., Gareil, N., Forges, H. de, Lescure, A., Latreche, L., Mercanti, V., Jollivet, F., Raposo, G., and Perez, F. (2012). Synchronization of secretory protein traffic in populations of cells. Nature methods. 10.1038/nmeth.1928.

15. Bastock, R., and Johnston, D.S. (2008). Drosophila oogenesis. Current biology : CB *18*, R1082-7. 10.1016/j.cub.2008.09.011.

16. Rabouille, C., Kuntz, D.A., Lockyer, A., Watson, R., Signorelli, T., Rose, D.R., Heuvel, M. van den, and Roberts, D.B. (1999). The Drosophila GMII gene encodes a Golgi alpha-mannosidase II. J Cell Sci *112*, 3319–3330. 10.1242/jcs.112.19.3319.

17. Vallotton, P., Oijen, A.M. van, Whitchurch, C.B., Gelfand, V., Yeo, L., Tsiavaliaris, G., Heinrich, S., Dultz, E., Weis, K., and Grünwald, D. (2017). Diatrack particle tracking software: Review of applications and performance evaluation. Traffic *18*, 840–852. 10.1111/tra.12530.

18. Meijering, E., Dzyubachyk, O., and Smal, I. (2012). Chapter nine Methods for Cell and Particle Tracking. Methods Enzymol *504*, 183–200. 10.1016/b978-0-12-391857-4.00009-4.

19. Smal, I., Yao, Y., Galjart, N., and Meijering, E. (2019). Facilitating Data Association In Particle Tracking Using Autoencoding And Score Matching. 2019 Ieee 16th Int Symposium Biomed Imaging Isbi 2019 *00*, 1523–1526. 10.1109/isbi.2019.8759418.

20. Chenouard, N., Smal, I., Chaumont, F. de, Maška, M., Sbalzarini, I.F., Gong, Y., Cardinale, J., Carthel, C., Coraluppi, S., Winter, M., et al. (2014). Objective comparison of particle tracking methods. Nat Methods *11*, 281–289. 10.1038/nmeth.2808.

21. Smal, I., and Meijering, E. (2015). Quantitative comparison of multiframe data association techniques for particle tracking in time-lapse fluorescence microscopy. Med Image Anal *24*, 163–189. 10.1016/j.media.2015.06.006.

22. Ritter, C., Wollmann, T., Lee, J.-Y., Imle, A., Müller, B., Fackler, O.T., Bartenschlager, R., and Rohr, K. (2021). Data fusion and smoothing for probabilistic tracking of viral structures in fluorescence microscopy images. Med Image Anal *73*, 102168. 10.1016/j.media.2021.102168.

23. Tinevez, J.-Y., Perry, N., Schindelin, J., Hoopes, G.M., Reynolds, G.D., Laplantine, E., Bednarek, S.Y., Shorte, S.L., and Eliceiri, K.W. (2017). TrackMate: An open and extensible platform for single-particle tracking. Methods *115*, 80–90. 10.1016/j.ymeth.2016.09.016.

24. Jaqaman, K., Loerke, D., Mettlen, M., Kuwata, H., Grinstein, S., Schmid, S.L., and Danuser, G. (2008). Robust single particle tracking in live cell time-lapse sequences. Nat Methods *5*, 695–702. 10.1038/nmeth.1237.

25. Allan, Caswell, D.B.;, Keim, T., Wel, N.C.; van der, Verweij, C.M.;, and W., R. (2019). soft-matter/trackpy: Trackpy v0.5.0. Zenodo. 10.5281/zenodo.4682814.

26. Wollmann, T., Ritter, C., Dohrke, J.N., Lee, J.-Y., Bartenschlager, R., and Rohr, K. (2019). Detnet: Deep Neural Network For Particle Detection In Fluorescence Microscopy Images. 2019 Ieee 16th Int Symposium Biomed Imaging Isbi 2019 *00*, 517–520. 10.1109/isbi.2019.8759234.

27. Newby, J.M., Schaefer, A.M., Lee, P.T., Forest, M.G., and Lai, S.K. (2018). Convolutional neural networks automate detection for tracking of submicron-scale particles in 2D and 3D. Proc National Acad Sci *115*, 9026–9031. 10.1073/pnas.1804420115.

28. Gudla, P.R., Nakayama, K., Pegoraro, G., and Misteli, T. (2017). SpotLearn: Convolutional Neural Network for Detection of Fluorescence In Situ Hybridization (FISH) Signals in High-Throughput Imaging Approaches. Cold Spring Harb Sym *82*, 57–70. 10.1101/sqb.2017.82.033761.

29. Fazeli, E., Roy, N.H., Follain, G., Laine, R.F., Chamier, L. von, Hänninen, P.E., Eriksson, J.E., Tinevez, J.-Y., and Jacquemet, G. (2020). Automated cell tracking using StarDist and TrackMate. F1000research *9*, 1279. 10.12688/f1000research.27019.2.

30. Yao, Y., Smal, I., Grigoriev, I., Akhmanova, A., and Meijering, E. (2020). Deep-learning method for data association in particle tracking. Bioinformatics *36*, 4935–4941. 10.1093/bioinformatics/btaa597.

31. Spilger, D.P.T.A.T. of P. in F.M.I.U.D.L.R. (2018). Deep particle tracker: automatic tracking of particles in fluorescence microscopy images using deep learning. In Deep Learning in Medical Image Analysis and Multimodal Learning for Clinical Decision Support.

32. Ershov, D., Phan, M.-S., Pylvänäinen, J.W., Rigaud, S.U., Blanc, L.L., Charles-Orszag, A., Conway, J.R.W., Laine, R.F., Roy, N.H., Bonazzi, D., et al. (2022). TrackMate 7: integrating state-of-the-art segmentation algorithms into tracking pipelines. Nat Methods *19*, 829–832. 10.1038/s41592-022-01507-1.

33. D'Alterio, C., Tran, D.D.D., Yeung, M.W.Y.A., Hwang, M.S.H., Li, M.A., Arana, C.J., Mulligan, V.K., Kubesh, M., Sharma, P., Chase, M., et al. (2005). Drosophila melanogaster Cad99C, the orthologue of human Usher cadherin PCDH15, regulates the length of microvilli. J Cell Biology *171*, 549–558. 10.1083/jcb.200507072.

34. Schlichting, K., Wilsch-Bräuninger, M., Demontis, F., and Dahmann, C. (2006). Cadherin Cad99C is required for normal microvilli morphology in Drosophila follicle cells. J. Cell Sci.*119*, 1184–1195. 10.1242/jcs.02831.

35. Dai, J., Estrada, B., Jacobs, S., Sánchez-Sánchez, B.J., Tang, J., Ma, M., Magadán-Corpas, P., Pastor-Pareja, J.C., and Martín-Bermudo, M.D. (2018). Dissection of Nidogen function in Drosophila reveals tissue-specific mechanisms of basement membrane assembly. PLoS Genetics *14*, e1007483. 10.1371/journal.pgen.1007483.

36. Wolfstetter, G., Dahlitz, I., Pfeifer, K., Töpfer, U., Alt, J.A., Pfeifer, D.C., Lakes-Harlan, R., Baumgartner, S., Palmer, R.H., and Holz, A. (2019). Characterization of Drosophila Nidogen/entactin reveals roles in basement membrane stability, barrier function and

nervous system patterning. Development (Cambridge, England) *146*, dev168948. 10.1242/dev.168948.

37. Zajac, A.L., and Horne-Badovinac, S. (2022). Kinesin-directed secretion of basement membrane proteins to a subdomain of the basolateral surface in Drosophila epithelial cells. Curr Biol. 10.1016/j.cub.2021.12.025.

38. Isabella, A.J., and Horne-Badovinac, S. (2016). Rab10-Mediated Secretion Synergizes with Tissue Movement to Build a Polarized Basement Membrane Architecture for Organ Morphogenesis. Dev. Cell *38*, 47–60. 10.1016/j.devcel.2016.06.009.

39. Karagöz, G.E., Acosta-Alvear, D., and Walter, P. (2019). The Unfolded Protein Response: Detecting and Responding to Fluctuations in the Protein-Folding Capacity of the Endoplasmic Reticulum. Csh Perspect Biol *11*, a033886. 10.1101/cshperspect.a033886.

40. Riedel, F., Gillingham, A.K., Rosa-Ferreira, C., Galindo, A., and Munro, S. (2016). An antibody toolkit for the study of membrane traffic in Drosophila melanogaster. Biol Open *5*, 987–992. 10.1242/bio.018937.

41. Ivan, V., Voer, G. de, Xanthakis, D., Spoorendonk, K.M., Kondylis, V., and Rabouille, C. (2008). Drosophila Sec16 Mediates the Biogenesis of tER Sites Upstream of Sar1 through an Arginine-Rich Motif. Mol Biol Cell *19*, 4352–4365. 10.1091/mbc.e08-03-0246.

42. Friggi-Grelin, F., Rabouille, C., and Therond, P. (2006). The cis-Golgi Drosophila GMAP has a role in anterograde transport and Golgi organization in vivo, similar to its mammalian ortholog in tissue culture cells. Eur J Cell Biol *85*, 1155–1166. 10.1016/j.ejcb.2006.07.001.

43. Sinka, R., Gillingham, A.K., Kondylis, V., and Munro, S. (2008). Golgi coiled-coil proteins contain multiple binding sites for Rab family G proteins. J. Cell Biol. *183*, 607–615. 10.1083/jcb.200808018.

44. Glashauser, J., Camelo, C., Hollmann, M., Backer, W., Jacobs, T., Sanchez, J.I., Schleutker, R., Förster, D., Berns, N., Riechmann, V., et al. (2023). Acute manipulation and real-time visualization of membrane trafficking and exocytosis in Drosophila. Dev. Cell *58*, 709-723.e7. 10.1016/j.devcel.2023.03.006.

45. Dmitrieva, M., Zenner, H.L., Richens, J., St Johnston, D. and Rittscher, J. (2019). Protein tracking by CNN-based candidate pruning and two-step linking with bayesian network. 2019 IEEE 29th Int. Workshop Machine Learning Signal Processing (MLSP) 1–6. 10.1109/mlsp.2019.8918873.

46. Jaiswal, A., Godinez, W.J., Eils, R., Lehmann, M.J., and Rohr, K. (2015). . Jaiswal, A., Godinez, W.J., Eils, R., Lehmann, M.J., and Rohr, K. (2015). Tracking virus particles in fluorescence microscopy images using multi-scale detection and multi-frame association. IEEE Trans. Image Processing. *24*, 4122–4136. 10.1109/tip.2015.2458174.

47. Kuhn, H.W. (1955). The Hungarian method for the assignment problem. Nav. Res. Logist. Q. *2*, 83–97. 10.1002/nav.3800020109.

48. Schindelin, J., Arganda-Carreras, I., Frise, E., Kaynig, V., Longair, M., Pietzsch, T., Preibisch, S., Rueden, C., Saalfeld, S., Schmid, B., et al. (2012). Fiji: an open-source platform for biological-image analysis. Nat. Methods *9*, 676–682. 10.1038/nmeth.2019.

49. Chenouard, N., Bloch, I., and Olivo-Marin, J.-C. (2013). Multiple hypothesis tracking for cluttered biological image sequences. IEEE Trans. Pattern Anal. *35*, 2736–3750. 10.1109/tpami.2013.97.

50. Doerflinger, H., Benton, R., Shulman, J.M., and St Johnston, D.(2003). The role of PAR-1 in regulating the polarised microtubule cytoskeleton in the Drosophila follicular epithelium. Development *130*, 3965–3975. 10.1242/dev.00616

51. Nashchekin, D., Fernandes, A.R., and St Johnston, D. (2016). Patronin/Shot cortical foci assemble the noncentrosomal microtubule array that specifies the Drosophila anterior-posterior Axis. Dev. Cell *38*, 61–72. 10.1016/j.devcel.2016.06.010.

52. Khanal, I., Elbediwy, A., Loza, M.D.C.D. de la, Fletcher, G.C., and Thompson, B.J. (2016). Shot and Patronin polarise microtubules to direct membrane traffic and biogenesis of microvilli in epithelia. J. Cell Sci. *129*, 2651–2659. 10.1242/jcs.189076.

53. Haigo, S.L., and Bilder, D. (2011). Global tissue revolutions in a morphogenetic movement controlling elongation. Science *331*, 1071–1074. 10.1126/science.1199424.

54. Lerner, D.W., McCoy, D., Isabella, A.J., Mahowald, A.P., Gerlach, G.F., Chaudhry, T.A., and Horne-Badovinac, S. (2013). A Rab10-dependent mechanism for polarized basement membrane secretion during organ morphogenesis. Dev. Cell *24*, 159–168. 10.1016/j.devcel.2012.12.005.

55. Bacallao, R., Antony, C., Dotti, C., Karsenti, E., Stelzer, E., and Simons, K. (1989). The subcellular organization of Madin-Darby canine kidney cells during the formation of a polarized epithelium. J. Cell Biol. *109*, 2817-32.

56. Toya, M., Kobayashi, S., Kawasaki, M., Shioi, G., Kaneko, M., Ishiuchi, T., Misaki, K., Meng, W., and Takeichi, M. (2016). CAMSAP3 orients the apical-to-basal polarity of microtubule arrays in epithelial cells. Proc. Natl Acad. Sci (USA) *113*, 332–337. 10.1073/pnas.1520638113.

57. Noordstra, I., Liu, Q., Nijenhuis, W., Hua, S., Jiang, K., Baars, M., Remmelzwaal, S., Martin, M., Kapitein, L.C., and Akhmanova, A. (2016). Control of apico-basal epithelial polarity by the microtubule minus-end-binding protein CAMSAP3 and spectraplakin ACF7. J. Cell Sci. *129*, 4278–4288. 10.1242/jcs.194878.

58. Trovisco, V., Belaya, K., Nashchekin, D., Irion, U., Sirinakis, G., Butler, R., Lee, J.J., Gavis, E.R., and Johnston, D.S. (2016). bicoid mRNA localises to the Drosophila oocyte anterior by random Dynein-mediated transport and anchoring. eLife *5*, e17537. 10.7554/elife.17537.

59. Soppina, V., Norris, S.R., Dizaji, A.S., Kortus, M., Veatch, S., Peckham, M., and Verhey, K.J. (2014). Dimerization of mammalian kinesin-3 motors results in super-processive motion. Proc Natl Acad. Sci. (USA) *111*, 5562–5567. 10.1073/pnas.1400759111.

60. Huckaba, T.M., Gennerich, A., Wilhelm, J.E., Chishti, A.H., and Vale, R.D. (2011). Kinesin-73 is a processive motor that localizes to Rab5-containing organelles*. J. Biol. Chem. *286*, 7457–7467. 10.1074/jbc.m110.167023.

61. Sharma, N., Low, S.H., Misra, S., Pallavi, B., and Weimbs, T. (2006). Apical targeting of syntaxin 3 is essential for epithelial cell polarity. J. Cell Biol. *173*, 937–948. 10.1083/jcb.200603132.

62. Beest, M.B.A. ter, Chapin, S.J., Avrahami, D., and Mostov, K.E. (2005). The role of syntaxins in the specificity of vesicle targeting in polarized epithelial cells. Mol. Biol. Cell *16*, 5784–5792. 10.1091/mbc.e05-07-0661.

63. Kreitzer, G., Schmoranzer, J., Low, S.H., Li, X., Gan, Y., Weimbs, T., Simon, S.M., and Rodriguez-Boulan, E. (2003). Three-dimensional analysis of post-Golgi carrier exocytosis in epithelial cells. Nat. Cell Biol. *5*, 126–136. 10.1038/ncb917.

64. Viktorinová, I., and Dahmann, C. (2013). Microtubule polarity predicts direction of egg chamber rotation in Drosophila. Curr. Biol. *23*, 1472–1477. 10.1016/j.cub.2013.06.014.

65. Barlan, K., Cetera, M., and Horne-Badovinac, S. (2017). Fat2 and Lar define a basally localized planar signaling system controlling collective cell migration. Dev. Cell *40*, 467-477.e5. 10.1016/j.devcel.2017.02.003.

66. Stedden, C.G., Menegas, W., Zajac, A.L., Williams, A.M., Cheng, S., Özkan, E., and Horne-Badovinac, S. (2019). Planar-polarized Semaphorin-5c and Plexin A promote the collective migration of epithelial cells in Drosophila. Curr. Biol. 10.1016/j.cub.2019.01.049.

67. Ren, X., Yang, Z., Xu, J., Sun, J., Mao, D., Hu, Y., Yang, S.-J., Qiao, H.-H., Wang, X., Hu, Q., et al. (2014). Enhanced specificity and efficiency of the CRISPR/Cas9 System with optimized sgRNA parameters in Drosophila. Cell Rep. *9*, 1151–1162. 10.1016/j.celrep.2014.09.044.

68. Port, F., Muschalik, N., and Bullock, S.L. (2015). Systematic evaluation of Drosophila CRISPR tools reveals safe and robust alternatives to autonomous gene drives in basic research. G3. *5*, 1493–1502. 10.1534/g3.115.019083.

69. Hayashi, S., Ito, K., Sado, Y., Taniguchi, M., Akimoto, A., Takeuchi, H., Aigaki, T., Matsuzaki, F., Nakagoshi, H., Tanimura, T., et al. (2002). GETDB, a database compiling expression patterns and molecular locations of a collection of Gal4 enhancer traps. Genesis *34*, 58–61. 10.1002/gene.10137.

70. Madan, V., Albacete, L.A., Jin, L., Scaturro, P., Watson, J.L., Muschalik, N., Begum, F., Boulanger, J., Bauer, K., Kiebler, M.A., et al. (2023). HEATR5B associates with dynein-dynactin and selectively promotes motility of AP1-bound endosomal membranes. EMBO J., 10.15252/embj.2023114473.

71. Buszczak, M., Paterno, S., Lighthouse, D., Bachman, J., Planck, J., Owen, S., Skora, A.D., Nystul, T.G., Ohlstein, B., Allen, A., et al. (2007). The Carnegie protein trap library: a versatile tool for Drosophila developmental studies. Genetics *175*, 1505–1531. 10.1534/genetics.106.065961.

72. Gepner, J., Li, M., Ludmann, S., Kortas, C., Boylan, K., Iyadurai, S.J.P., McGrail, M., and Hays, T.S. (1996). Cytoplasmic dynein function is essential in Drosophila melanogaster. Genetics *142*, 865–878. 10.1093/genetics/142.3.865.

73. Tanaka, T., and Nakamura, A. (2008). The endocytic pathway acts downstream of Oskar in Drosophila germ plasm assembly. Development *135*, 1107–1117. 10.1242/dev.017293.

74. Dmitrieva, M., Lefebvre, J., Peñas, K. delas, Zenner, H.L., Richens, J., St Johnston, D., and Rittscher, J. (2020). Short trajectory segmentation with 1D UNET framework: application to secretory vesicle dynamics. 2020 IEEE 17th Int. Symp. Biomed. Imaging (ISBI), 891–894. 10.1109/isbi45749.2020.9098426.

75. Yaniv, Z., Lowekamp, B.C., Johnson, H.J., and Beare, R. (2018). SimpleITK image-analysis notebooks: a collaborative environment for education and reproducible research. J. Digit. Imaging *31*, 290–303. 10.1007/s10278-017-0037-8.

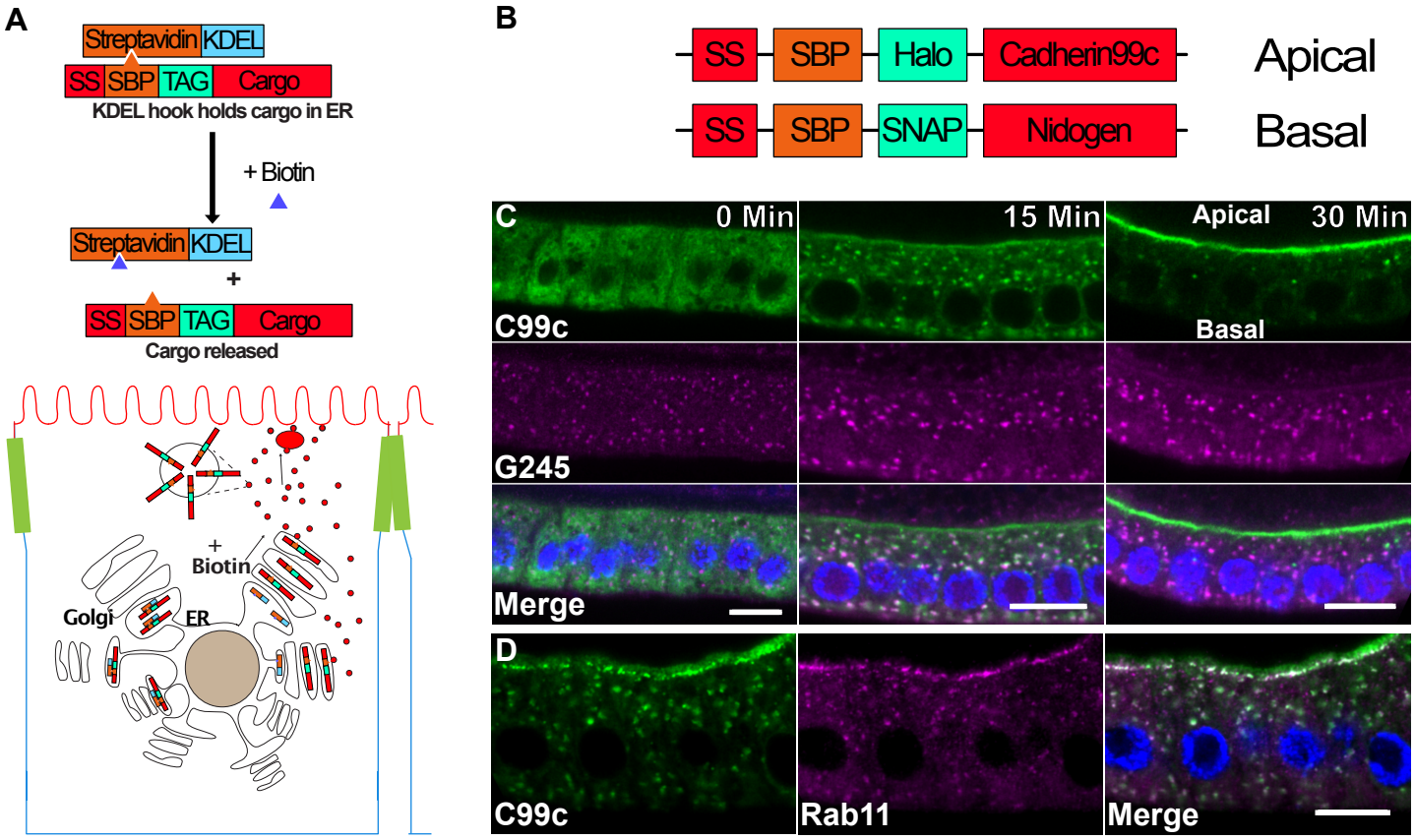

Figure 1. The RUSH system

A) Diagram of the RUSH system. The Halo-tagged cargo is retained in the ER by the binding of the Streptavidin binding peptide (SBP) to Streptavidin (StrepA), which is fused to the ER retention signal, KDEL. The cargo is synchronously released upon the addition of biotin, which outcompetes SBP for binding to Streptavidin.

B) Diagram of the tagged cargo constructs used in this study. A signal sequence is followed by the SBP, then the tag, and the cargo. Cadherin 99C (Cad99c) was used as an apical cargo and Nidogen (Ndg) as a basal cargo.

C) Time course of SBP-Halo-Cadherin99C trafficking in fixed samples. At 0 minutes, Cad99c localises to the ER throughout the cytoplasm. 15 minutes after release from the ER with biotin, Cad99c (green) has accumulated in the Golgi, marked by Golgin245 (magenta). By 30 minutes, almost all Cad99c has reached the apical membrane. Scale bar 10 µm.

D) 25 minutes after release from the ER, Cad99c (green) localises to sub-apical puncta that are labelled by Rab11 (magenta). Scale bar 10 µm.

In all figures with a cross-section of the follicle cells, apical is toward the top of the image. And basal toward the bottom.

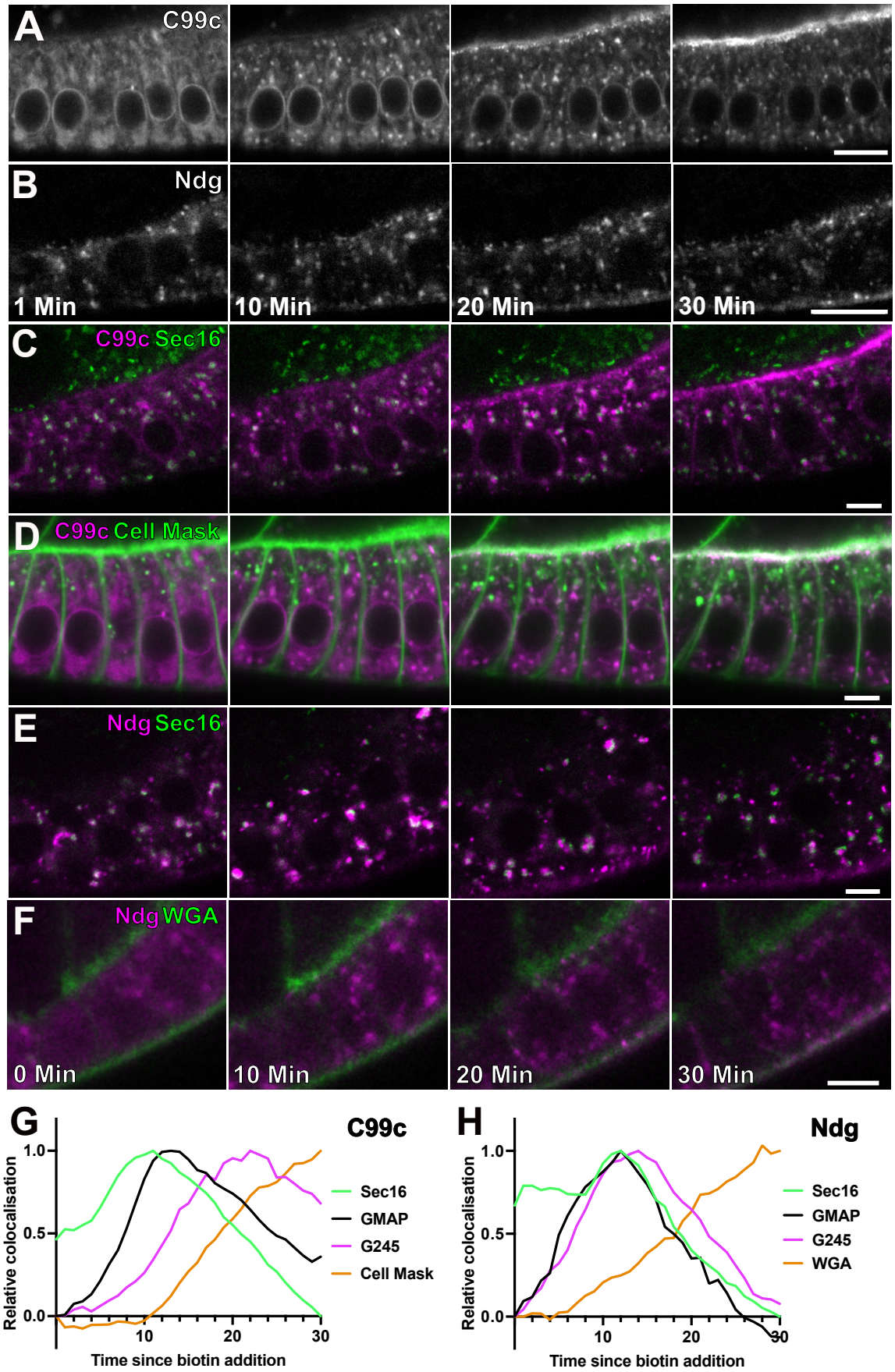
A
C99c
B
Ndg
1 Min
10 Min
20 Min
30 Min
C
C99c Sec16
D
C99c Cell Mask
E
Ndg Sec16
F
Ndg WGA
0 Min
10 Min
20 Min
30 Min
G
C99c
Relative colocalisation
1.0
0.5
0.0
10
20
30
Time since biotin addition
Sec16
GMAP
G245
Cell Mask
H
Ndg
Relative colocalisation
1.0
0.5
0.0
10
20
30
Time since biotin addition
Sec16
GMAP
G245
WGA

Figure 2. Time course of Cad99c and Nidogen secretion

A-B) Stills from RUSH movies of SBP-Halo-Cadherin 99c (A) and SBP-SNAP-Nidogen (B) trafficking in the follicle cells after release from the ER. Cad99c is shown in an early stage 9 egg chamber, and the Ndg in a stage 8 egg chamber. Scale bars 10 µm. Time indicates minutes since the addition of biotin. Cad99c is labelled with Halo-OregonGreen, and Ndg with SNAP-SiR. The large cytoplasmic puncta visible 10 minutes after cargo release are Golgi ministacks.

C) Stills from a RUSH movie of SBP-Halo-Cadherin 99c (labelled with Halo-JF646; magenta) in cells expressing GFP-Sec16 (green), which marks ER exit sites. Scale bars 5 µm. Cad99c co-localises with Sec16 at ER exit sites after 10 minutes, and by 20 minutes is predominantly localised to the Golgi, which lie adjacent to the ER exit sites (See supplementary Figure 2).

D) Stills from a RUSH movie of SBP-Halo-Cadherin 99c (magenta) in cells in which the plasma membrane is labelled with CellMask™. Some Cad99c has already reached the apical membrane by 20 minutes and much more is localised apically at 30 minutes.

E) Stills from a movie of SBP-Halo-Ndg RUSH in cells expressing GFP-Sec16. Some colocalisation of Ndg with Sec16 can be seen at time 0, presumably as Ndg is a soluble protein present in the ER, and is able to partly accumulate at the ER exit sites. Most Nidogen localises at ER exit sites after ten minutes and in the adjacent Golgi mini-stacks after 20 minutes.

F) Stills from a movie of SBP-Halo-Ndg RUSH (SNAP-SiR; magenta) in cells labelled with alexa488-wheatgerm agglutinin (WGA; green), which labels the basal membrane. Scale bars 5 µm. Colocalisation of Ndg with WGA can be seen from 20 minutes, and is stronger at 30 minutes as Ndg has been secreted and bound to the ECM.

G) Graph showing the extent of Cad99c colocalisation with GFP-Sec16 (ER exit sites), GFP-GMAP (*cis*-Golgi), GFP-G245 (*trans*-Golgi and TGN) and CellMask™ (plasma membrane) over time. Cad99c colocalisation with Sec16 peaks at 11 minutes after biotin addition, its colocalisation with GMAP peaks between 12-14 minutes and with G245 is at 22-23 minutes. Cad99c starts to co-localise with CellMask™ at 11 minutes and increases over time. The number of movies used for each marker is detailed in the materials and methods.

H) Graph showing the extent of Nidogen colocalisation with GFP-Sec16, GFP-GMAP, GFP-Golgin245 and with WGA, which marks the basal membrane. Ndg colocalisation with Sec16 is already high before biotin addition, and peaks at 12 minutes after biotin addition, which is also when the peak colocalisation with GMAP occurs, indicating rapid transit of Ndg from the ER exit sites to the *cis*-Golgi. Peak Ndg colocalisation with G245 is at 14 minutes, again indicating rapid transit through the Golgi. Basal Ndg signal is observable from 6 minutes, and increases over time. It is important to note that as a soluble protein, the Ndg present in the basement membrane is not necessarily from the egg chamber being observed. The number of movies used for each marker is detailed in the materials and methods.

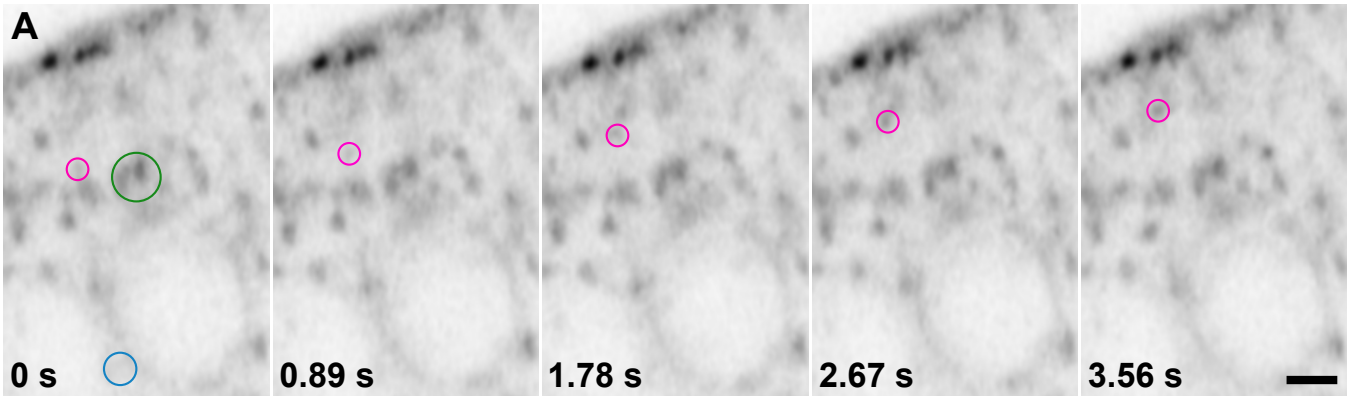

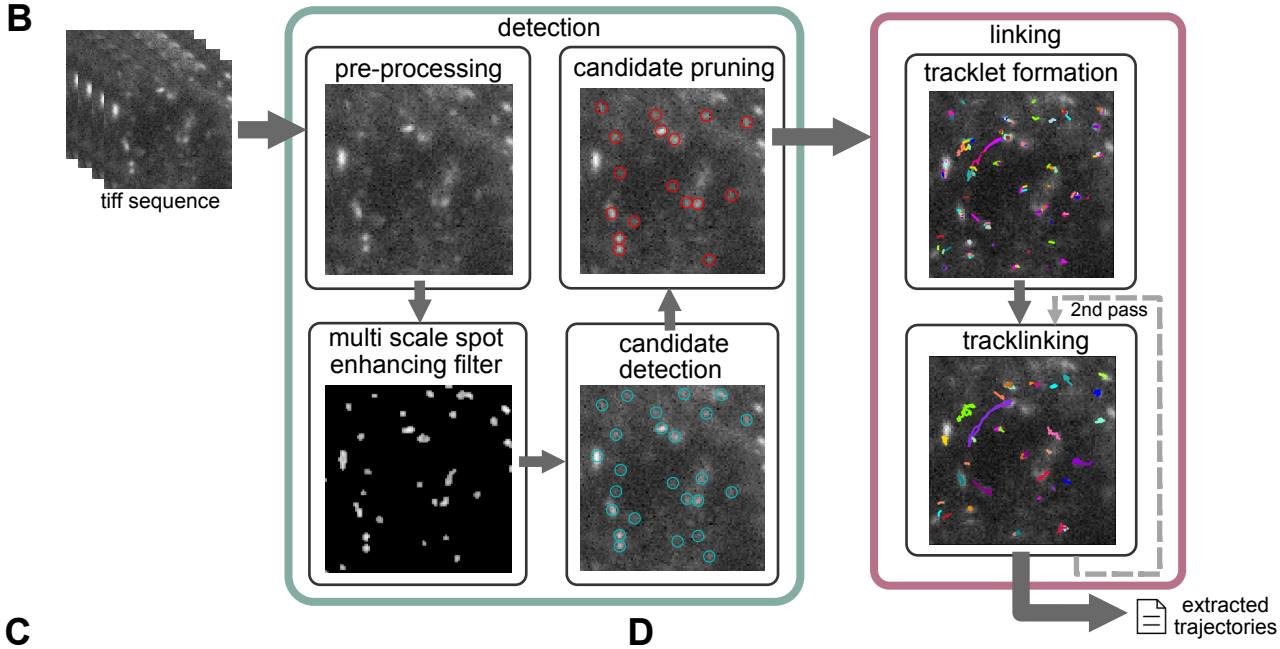

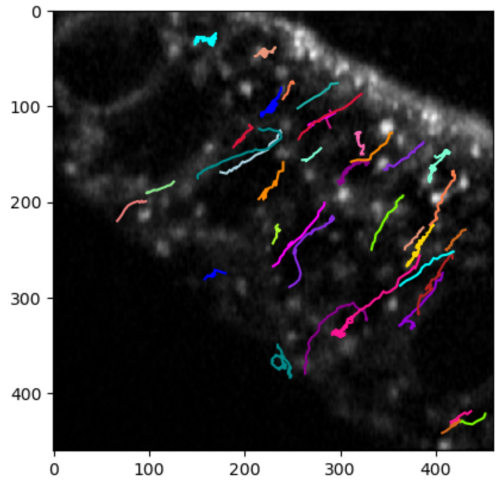

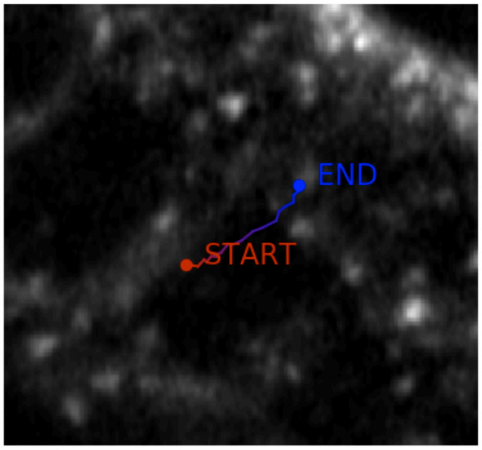

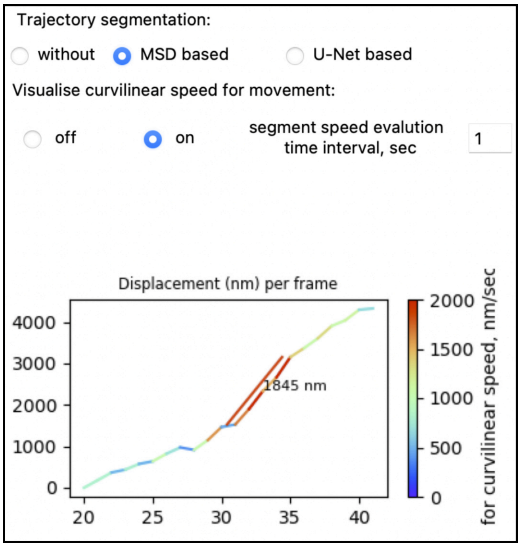

F

Net distance travelled	4325.16 nm
Maximum distance travelled	4325.16 nm
Total trajectory time	4.66667 sec
Net orientation	174 degrees
Mean brightness (normalised)	0.07934
Mean curvilinear speed: average	1086.0 nm/sec
Mean straight-line speed: average	927.0 nm/sec
Mean curvilinear speed: moving	1086.0 nm/sec
Mean straight-line speed: moving	927.0 nm/sec
Max curvilinear speed over a segment : moving	1845.0 nm/sec

Figure 3. The MSP-tracker and viewer analysis pipeline

A) Examples of frames from a Cad99c RUSH movie, highlighting both particles of interest (magenta circles), background/ER signal (blue circle), and Golgi mini-stacks (green circle). Scale bar 2 µm.

B) Workflow for MSP-Tracker showing the steps taken from .tiff file to trajectories.

C) An example of the output of MSP-viewer showing the trajectories of Cad99c vesicles overlaid onto a movie still. The image was obtained using the trajectories:save image command in the mspviewer software.

D) Example of a Cad99c track as seen in the “trackviewer” window of MSP-viewer.

E) Example of the trajectory segmentation section of the “trackviewer” window in MSP-viewer. The marked speed is the fastest segment of the track over a 1 second time interval.

F) Trajectory information as viewed in the “trackviewer” window. These data are output into a .csv file using the trajectories:save info to csv function.

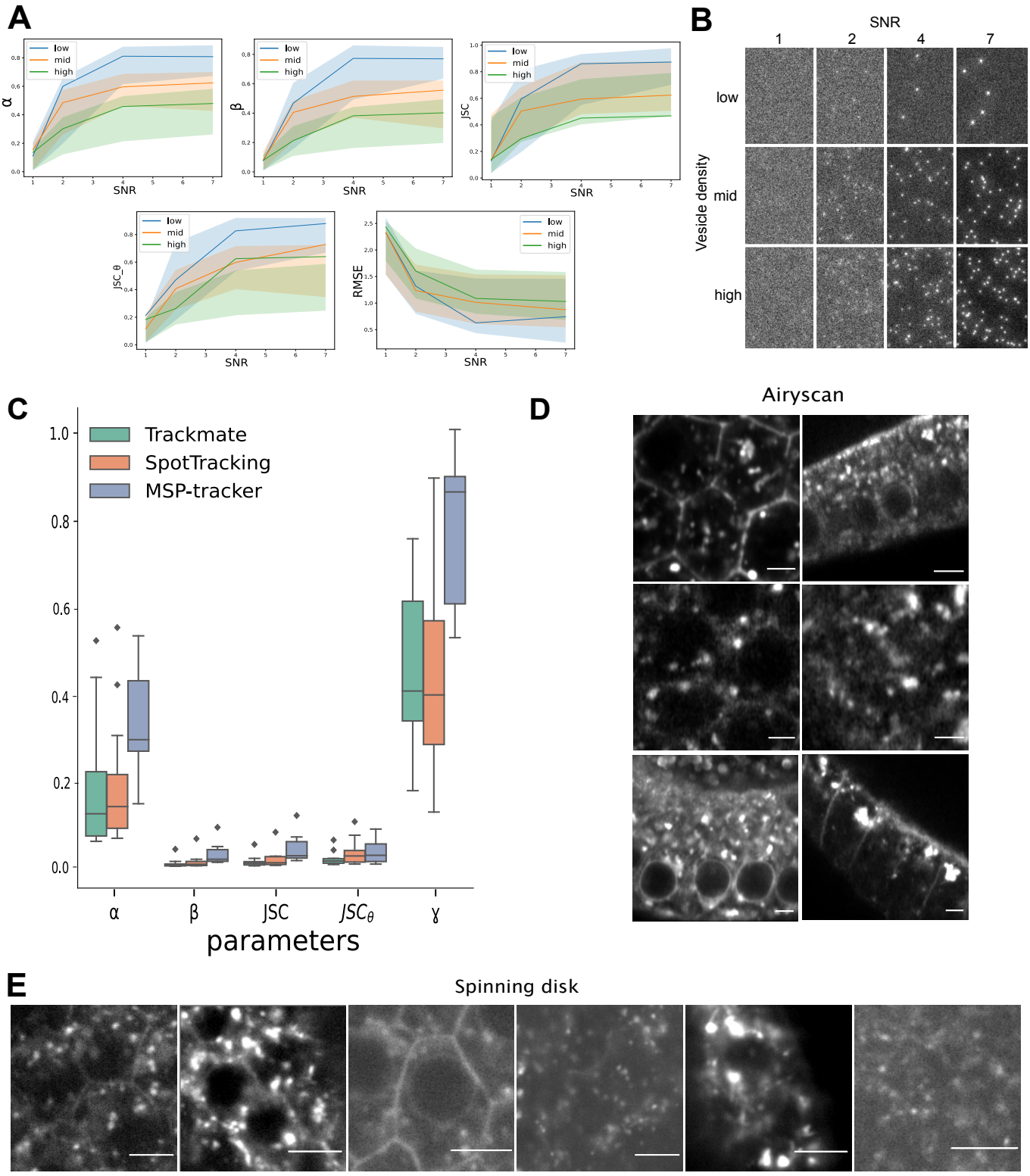

Figure 4. Evaluation of the MSP-tracker

A) Performance of the proposed MSP-tracker evaluated on the particle tracking challenge data [20]**.** The performance is evaluated by α and β measures, the Jaccard similarity coefficient for track points JSC, the Jaccard similarity coefficient for the entire tracks JSC_θ and root mean square error (RMSE) of matching points in the paired tracks. The lines represent the MSP-tracker results and coloured areas refer to the range of the results presented in the original challenge paper [20].

B) Frame examples of the particle tracking challenge data.

C) Performance of the proposed MSP-tracker, Trackmate and SpotTracking evaluated on the original data. Linking performance is evaluated by α and β measures, the Jaccard similarity coefficient for track points JSC, as well as for the entire tracks JSC_θ and a fraction of paired up tracks γ.

D) Frame examples of Airyscan data in the original dataset. Scale bars 5 μm.

E) Frame examples of spinning disc data in the original dataset. Scale bars 5 μm.

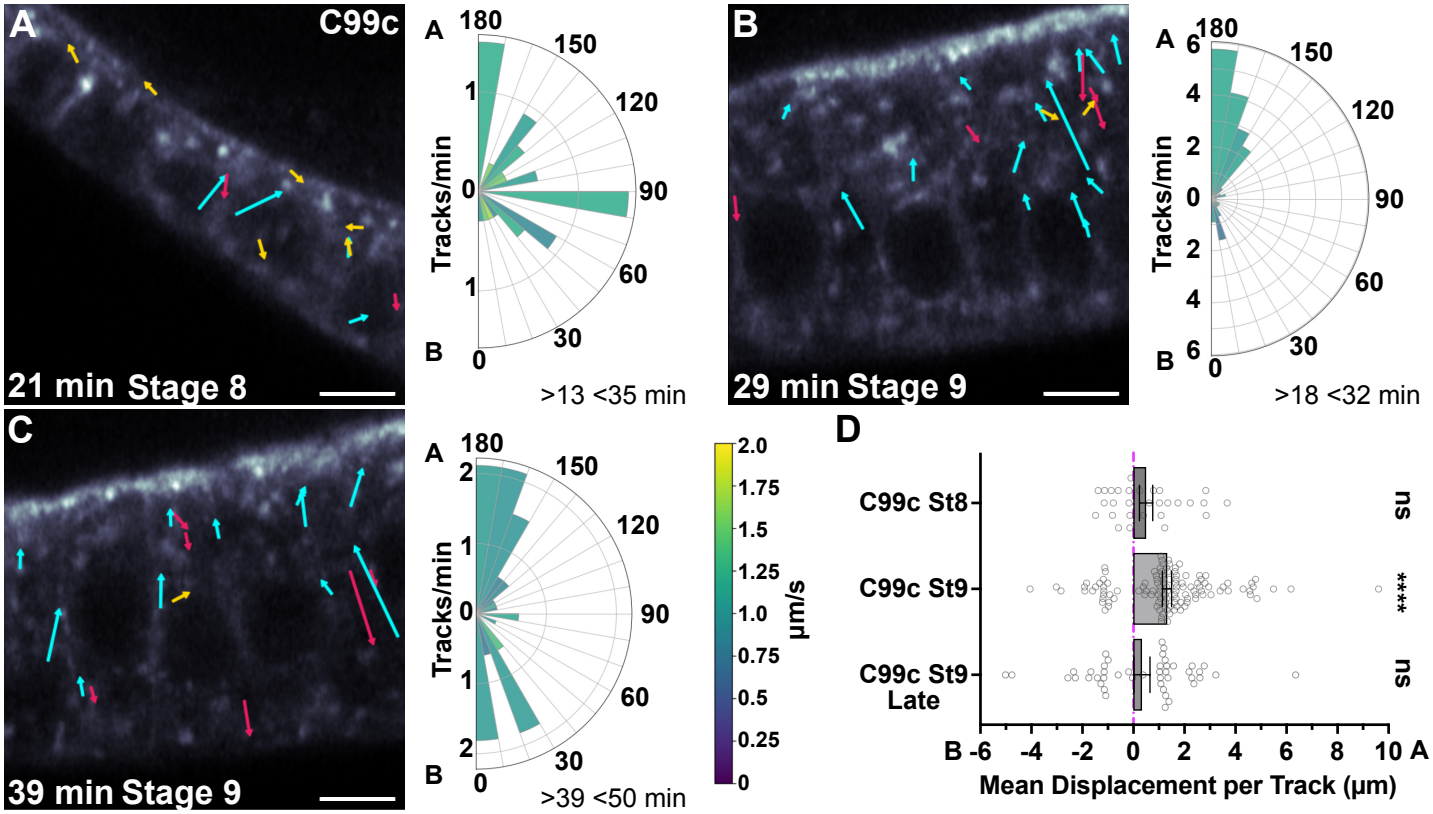

Figure 5. Cad99c tracks are apically biased.

A) Tracks from representative movie of Cad99c trafficking in a stage 8 egg chamber 21 minutes after biotin addition. The polar histogram on the right shows the orientation of Cad99c tracks from 3 Airyscan movies. This and the following polar histograms represent the number of tracks that travelled at least 1 µm in each 10˚ direction, with apical (A) at the top and basal (B) at the bottom. The plots are normalised to show tracks per minute and speeds are colour coded according to the key. All movies were collected at 4.5 fps. Cad99c was labelled with Halo-JF549. Scale bars are 5 µm.

B) Tracks from representative movie of Cad99c trafficking in a stage 9 egg chamber, 29 minutes after biotin addition. The polar plot represents data from 5 Airyscan movies and shows a strong apical bias in the direction of Cad99c vesicle movements.

C) Tracks from representative movie of Cad99c trafficking in a stage 9 egg chamber 39 minutes after biotin addition. The polar plot represents data from 3 Airyscan movies. By this timepoint, the strong apical bias is lost, as the exocytosis of C99c is balanced by endocytosis.

D) Graph showing the net displacement of Cad99c vesicle tracks along the apical-basal axis, with positive displacement towards apical (A), and negative towards basal (B). The bar shows the mean, and the error bars the s.e.m. Individual tracks are indicated by the small circles. The mean displacement for stage 8 is 0.49 µm ±0.26 (s.e.m), and for stage 9 is 1.32 µm ±0.18 (s.e.m). Significance was calculated using a Wilcoxon Signed-Rank test for comparing the displacement to zero.

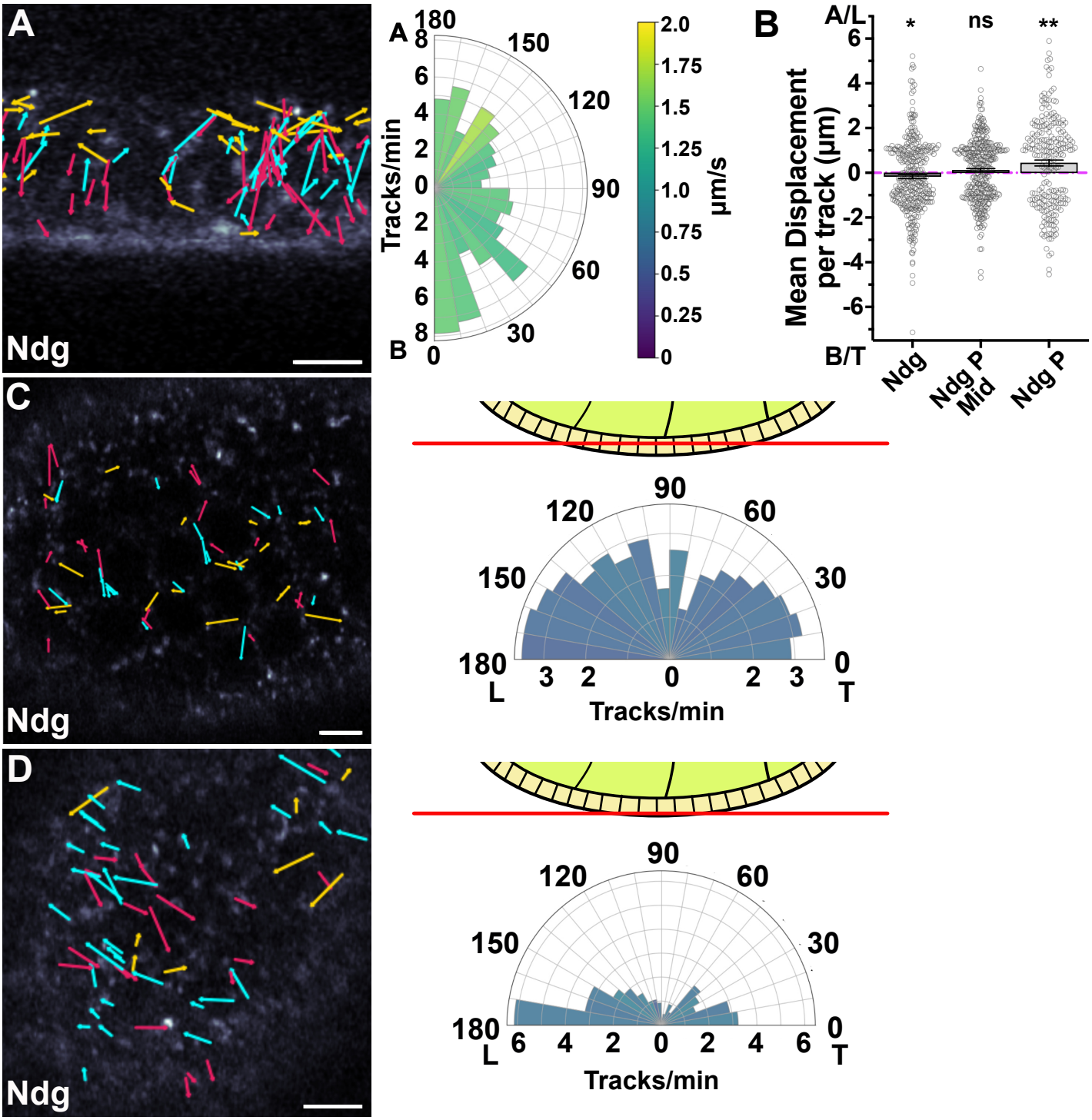

Figure 6. Analysis of Ndg tracks reveals planar polarised transport basally.

A) Tracks from a representative movie of Ndg trafficking in a stage 8 egg chamber 23 minutes after biotin addition. The polar plot on the right represents data from 3 Airyscan movies and shows a weak bias towards the basal side of the cell. Movies were taken at 3.7 fps.

B) Graph showing the net displacement of Ndg vesicle tracks along the apical-basal axis (A, B; lefthand column) and along the leading edge to trailing edge axis (L,T) in the middle of the cell (middle column) and on the basal side of the cell (righthand column). The bars and error bars show the means and s.e.m. Individual tracks are indicated by the small circles. P indicates planar. Mean displacement towards basal is 0.17 µm ±0.09 (s.e.m). The mean displacement for planar polarised tracks in the middle of the cell was 0.11 µm ±0.07 (s.e.m) towards the leading edge, and for the basal tracks, 0.44 µm ±0.13 (s.e.m) towards the leading edge. Significance was calculated using a Wilcoxon Signed-Rank test for comparing the displacement to zero .

C) Ndg tracks in a transverse section through the middle of the follicle cell epithelium (see diagram). The polar plot represents data from 3 Airyscan movies taken at 2.3 fps. The Leading and trailing (L and T) directions of the egg chamber's rotation are indicated.
D) Ndg tracks in a transverse section through the basal section of the follicle cell epithelium. The polar plot represents data from 3 Airyscan movies taken at 2.3 fps. The leading and trailing (L and T) directions of follicle cell migration are indicated. Most tracks are directed towards the leading edge.

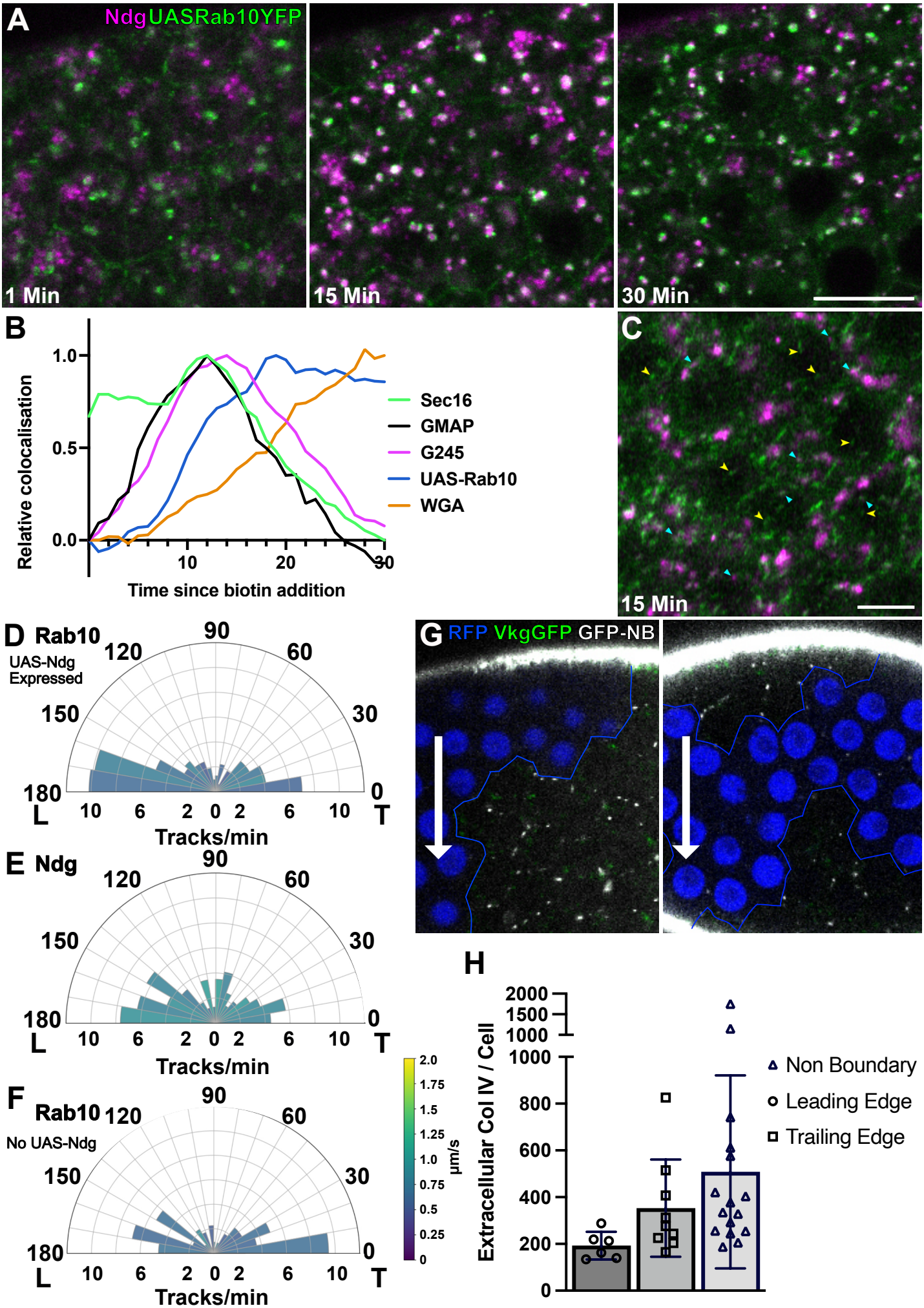
A
NdgUASRab10YFP
1 Min
15 Min
30 Min
B
Relative colocalisation
1.0
0.5
0.0
10
20
30
Time since biotin addition
Sec16
GMAP
G245
UAS-Rab10
WGA
C
15 Min
D Rab10
UAS-Ndg
Expressed
90
120
60
150
30
180
0
L
T
10 6 2 0 2 6 10
Tracks/min
E Ndg
90
120
60
150
30
180
0
L
T
10 6 2 0 2 6 10
Tracks/min
F Rab10
No UAS-Ndg
90
120
60
150
30
180
0
L
T
10 6 2 0 2 6 10
Tracks/min
2.0
1.75
1.5
1.25
1.0
0.75
0.5
0.25
0
µm/s
G RFP VkgGFP GFP-NB
H
Extracellular Col IV / Cell
2000
1500
1000
1000
800
600
400
200
0
Non Boundary
Leading Edge
Trailing Edge

Figure 7. Ndg is transported in Rab10 positive vesicles.

A) Stills from a RUSH movie of SBP-SNAP-Nidogen (labelled with SNAP-SiR; magenta) in cells expressing UAS-Rab10-YFP (green). Scale bar 5 µm. Ndg colocalises with Rab10 in large vesicular structures 15 minutes after biotin addition, but this colocalisation has largely disappeared by 30 minutes.

B) Graph showing the extent of Nidogen colocalisation with GFP-Sec16, GFP-GMAP, GFP-Golgin245, UAS-Rab10-YFP and basal WGA over time. Ndg colocalisation with Rab10 peaks at 19 minutes, after the peak with G245, indicating Ndg leaves the Golgi and transits through a Rab10 positive compartment on its way out of the cell. The graph is the same as Figure 2H, but with the addition of UAS-Rab10-YFP to show where it fits into the pathway.

C) Still from an Airyscan movie of the basal side of cells expressing UAS-Rab10-YFP and Ndg. The yellow arrowheads indicate Rab10 vesicles, Cyan arrowheads indicate Rab10 vesicles that contain Ndg.

D) A polar plot of Rab10 tracks from movies at the basal side of cells also expressing SNAP-Ndg. Rab10 vesicle movements show a bias to the leading edge. The polar plot represents tracks from two Airyscan movies.

E) A polar plot of Ndg tracks from the same movies as D), also showing a leading edge bias.

F) A polar plot of Rab10 tracks from movies of cells not expressing SNAP-Ndg, showing a bias towards the trailing edge. The plot represents tracks from two Airyscan movies.

G) Stills from movies looking at Collagen IV secretion in Vkg-GFP clones. Double RFP (Vkg-GFP negative) cells are marked in blue, and the clone boundary is also marked by a blue line. The direction of migration is indicated for each movie with an arrow. Extracellular Collagen IV is labelled with GFP-booster conjugated to Atto647n. Intra- and extracellular Collagen IV is marked with GFP.

H) Quantification of extracellular Collagen IV levels at the leading and trailing edges of cells, from movies such as those represented in G). Cells whose leading edges contacted the double RFP non-expressing cells were used to measure the amount of Collagen IV secreted at the leading edge, and cells with trailing edges contacting the non-expressing clone were used to measure Collagen IV secretion at trailing edges. Non-boundary cells were used to measure the total amount of Collagen IV secreted where the leading and trailing edges of neighbouring cells meet. The majority of the Collagen IV is secreted from the trailing edge.

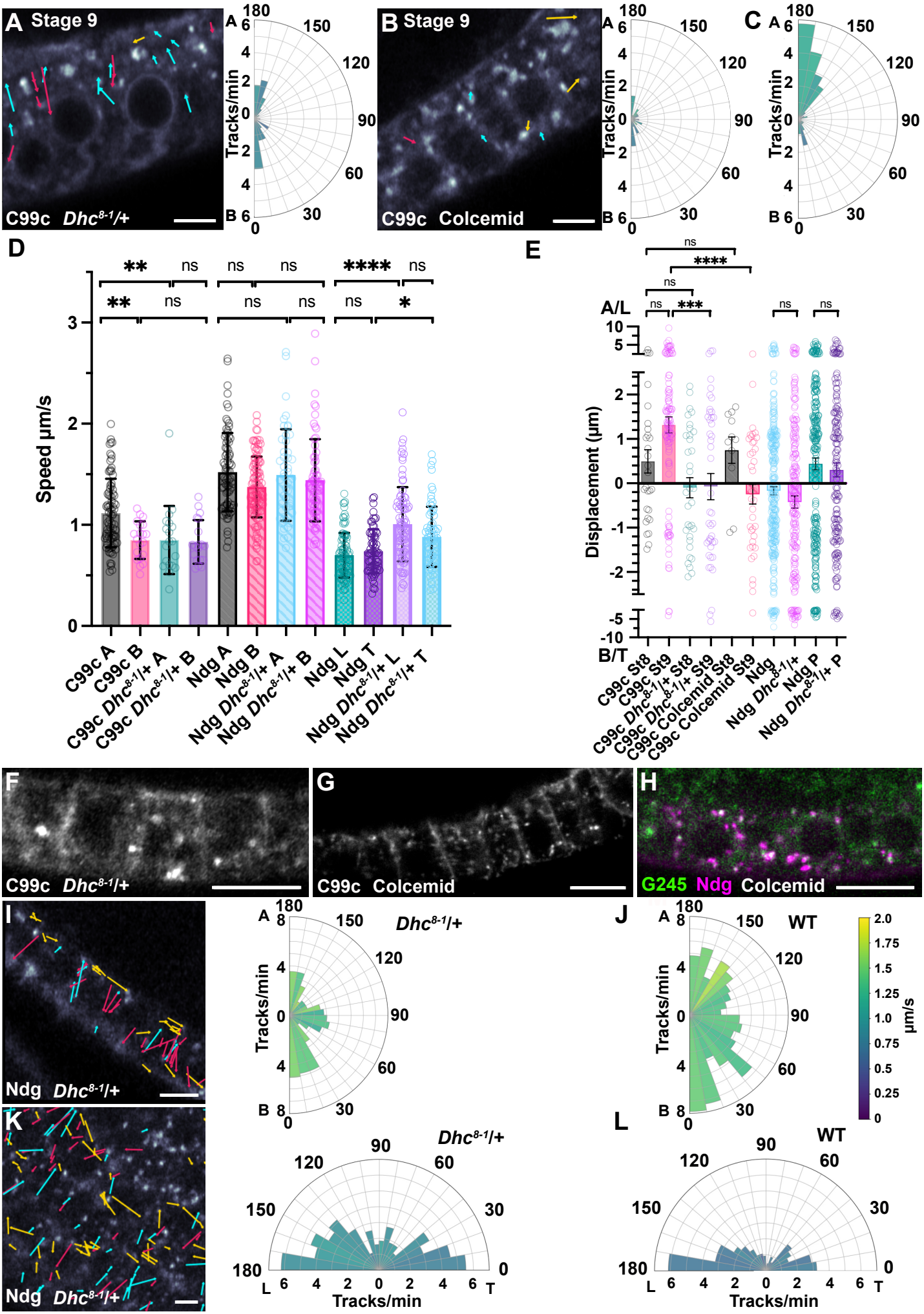
A Stage 9
C99c Dhc8-1/+
B Stage 9
C99c Colcemid
C
Tracks/min
D
Speed µm/s
C99c A
C99c B
C99c Dhc8-1/+ A
C99c Dhc8-1/+ B
Ndg A
Ndg B
Ndg Dhc8-1/+ A
Ndg Dhc8-1/+ B
Ndg L
Ndg T
Ndg Dhc8-1/+ L
Ndg Dhc8-1/+ T
E
A/L
B/T
Displacement (µm)
C99c St8
C99c St9
C99c Dhc8-1/+ St8
C99c Dhc8-1/+ St9
C99c Colcemid St8
C99c Colcemid St9
Ndg
Ndg Dhc8-1/+
Ndg P
Ndg Dhc8-1/+ P
F
C99c Dhc8-1/+
G
C99c Colcemid
H
G245 Ndg Colcemid
I
Ndg Dhc8-1/+
Dhc8-1/+
J
WT
µm/s
K
Ndg Dhc8-1/+
Dhc8-1/+
L
WT
Tracks/min

Figure 8. The effects of a slow dynein mutant and microtubule depolymerisation on Cad99c and Ndg trafficking.

A) Tracks from a representative movie of Cad99c trafficking in a *Dhc*$^{8-1}$ heterozygous stage 9 egg chamber 13 minutes after biotin addition. The polar plot on the right represents data from 3 Airyscan movies and shows the loss of the apical bias in Cad99c vesicle movements seen in WT egg chambers. Scale bar 5 µm.

B) Tracks from a representative movie of Cad99c trafficking in a stage 9 egg chamber 26 minutes after biotin addition that has been treated with colcemid to depolymerise microtubules. The polar plot on the right represents data from 4 movies. Scale bar 5 µm.

C) A polar plot of Cad99c tracks in wild-type stage 9 egg chambers for comparison with (A) and (B). The plot represents data from 5 movies.

The scales in A) B) and C) are the same to allow for easy comparison.

D) Graph showing the maximum curvilinear speeds (over a segment) of Cad99c and Ndg vesicles travelling apically or basally in wild-type and *Dhc*$^{8-1}$/+ flies and for planar polarised Ndg tracks along the basal surface. Apical (A), Basal (B), Leading Edge (L), and Trailing Edge (T). Cad99c vesicles move significantly faster apically than basally, and significantly faster than apical tracks in the *Dhc*$^{8-1}$/+ background. The *Dhc*$^{8-1}$ mutation has no effect on the speeds of Ndg vesicle movements along the apical-basal axis, but increases the the speed of planar-polarised vesicle movements at the basal side of the cell. The bars and error bars represent the means and standard deviations and the circles represent individual tracks. Statistical significance determined by Kruskal-Wallis test using Dunn's multiple comparisons test, with significant differences between conditions indicated: * = $p < 0.05$, ** = $p < 0.01$, **** = $p < 0.0001$.

E) Graph showing the mean displacement of Cad99c and Ndg tracks in wild-type and *Dhc*$^{8-1}$/+. Positive displacement is towards the apical side (A) of the cell, with negative values indicating displacement towards the basal side (B). The last two columns show the displacement of Ndg vesicles on the basal surface towards the leading edge of the cell (L). Bars and error bars represent the means and standard errors of the means (s.e.m), and circles represent individual tracks. The y axis is compressed at large displacement values to present the data more clearly. Statistical significance for the C99c dataset determined by Kruskal-Wallis test using Dunn's multiple comparisons test, with significant differences between conditions indicated. Statistical significance for the Ndg pairs determined by Mann-Whitney test. * = $p < 0.05$, ** = $p < 0.01$, **** = $p < 0.0001$.

F) An image of Cad99c RUSH in a *Dhc*$^{8-1}$/+ background, taken 43 min after biotin addition. Cad99c has been delivered to the lateral membrane, but not the apical membrane. Scale bar 10 µm.

G) A projection of a Z-stack from a movie of Cad99c RUSH in a colcemid treated egg chamber. Stack taken 54 minutes after biotin addition. Cad99c has been delivered to the lateral membrane, but not the apical membrane. Scale bar 10 µm.

H) Image from a movie of Ndg trafficking in a colcemid-treated stage 8 egg chamber expressing GFP-G245. The image was taken 30 min after biotin addition and shows that most Ndg is still trapped in the Golgi ministacks. Scale bar 10 µm.

I) Tracks from representative movie of Ndg trafficking in a stage 8 *Dhc*$^{8-1}$/+ egg chamber taken 24 minutes after biotin addition. Scale bar 5 µm. The polar plot on the right represents 3 movies and shows the number of tracks per minute.

J) A polar plot showing the number of Ndg tracks per minute in WT stage 8 egg chambers for comparison with (I).

Figure 8. The effects of a slow dynein mutant and microtubule depolymerisation on Cad99c and Ndg trafficking. -continued

K) Tracks from representative movie of Ndg trafficking at the basal side of a stage 8 *Dhc*$^{8-1}$/+ egg chamber taken 22 minutes after biotin addition. Scale bar 5 µm. The polar plot represents 2 movies and shows the number of tracks per minute.

L) A polar plot showing the number of Ndg tracks per minute in wild-type stage 8 egg chambers for comparison with (K)

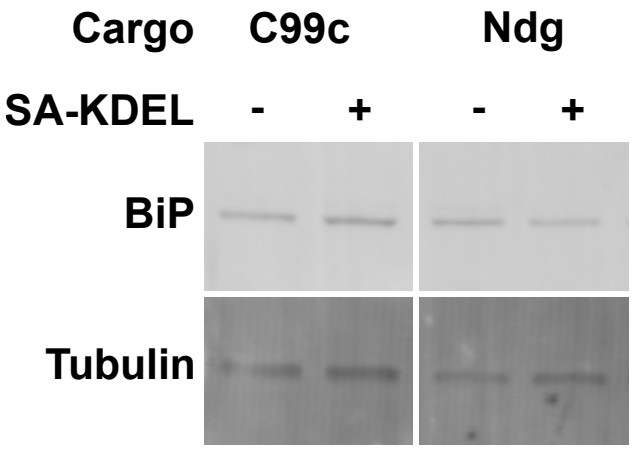

Supplement for Figure 1 – RUSH does not cause ER stress.

BiP expression in egg chambers expressing the Cad99c and Ndg RUSH constructs, with or without the 2x Streptavidin-KDEL insertions that retain the cargoes in the ER. Tubulin was used as a loading control. BiP levels do not change when the 2x Streptavidin-KDEL hook was expressed to retain the cargoes in the ER, indicating that trapping the cargoes does not cause ER stress.

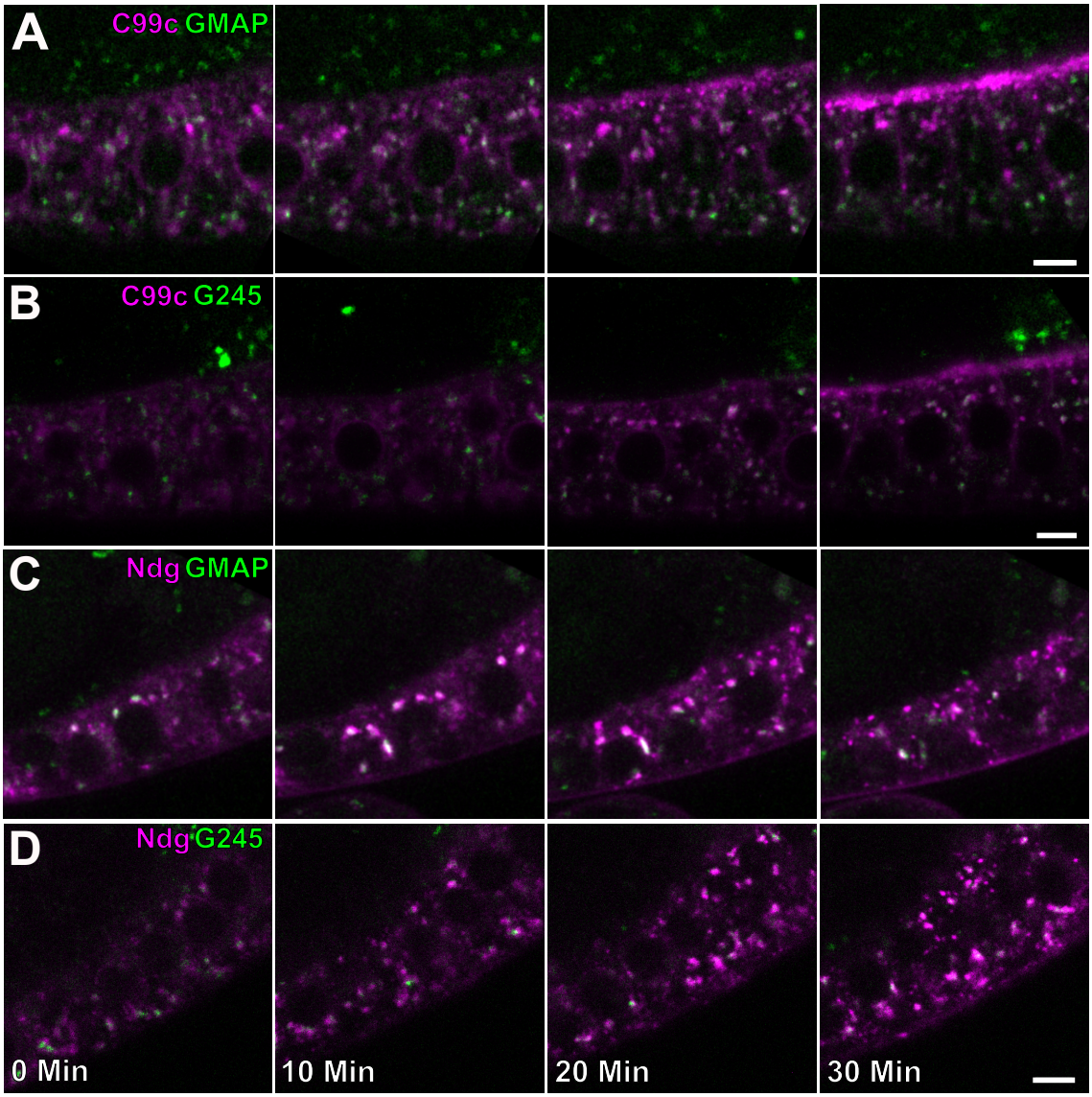

Supplement for Figure 2 – Time course of Cad99c and Nidogen secretion.
A) Stills at different time points are biotin addition from a RUSH movie of SBP-Halo-Cadherin 99c (magenta) trafficking in cells expressing GFP-GMAP (*cis*-Golgi), GFP-Golgin245 (*trans*-Golgi and TGN) as secretory pathway markers. Scale bars 5 µm.
B) Stills from a RUSH movie of SBP-SNAP-Nidogen trafficking in cells expressing GFP-GMAP, or GFP-Golgin245 as secretory pathway markers. Scale bars 5 µm.

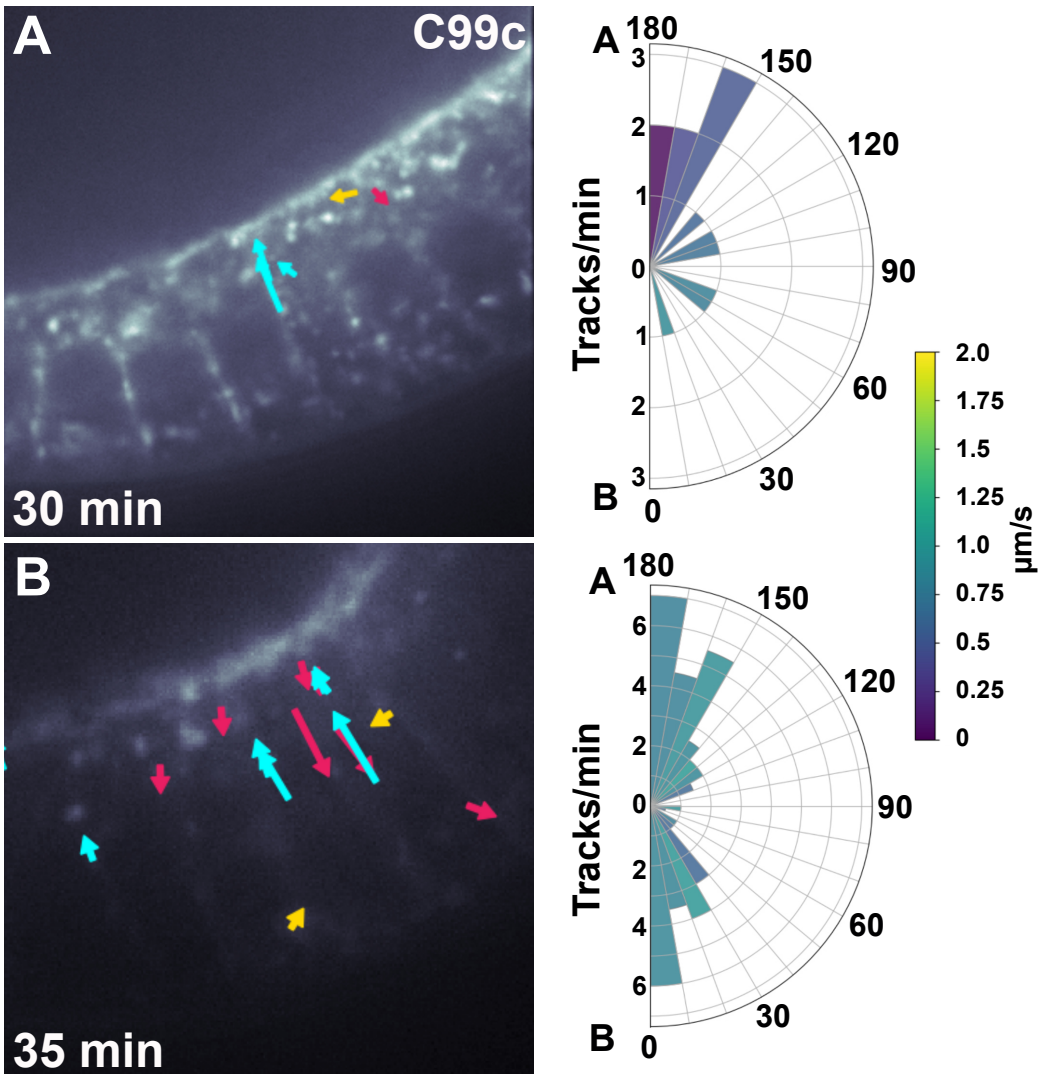

Supplement for Figure 5 – Spinning disc imaging of Cad99c trafficking

A) Tracks from representative movie taken on a spinning disc microscope of Cad99c trafficking in a stage 9 egg chamber, 30 minutes after biotin addition. The polar plot on the right shows the strong apical bias in the direction of the tracks. Movies were taken at 2 fps using a custom-built spinning disc system

B) Tracks from representative movie taken on a spinning disc microscope of Cad99c trafficking in a stage 9 egg chamber, 35 minutes after biotin addition. The polar plot on the right represents data from 2 spinning disc movies and shows that the strong apical bias has disappeared, as the exocytosis of C99c is now balanced by endocytosis.

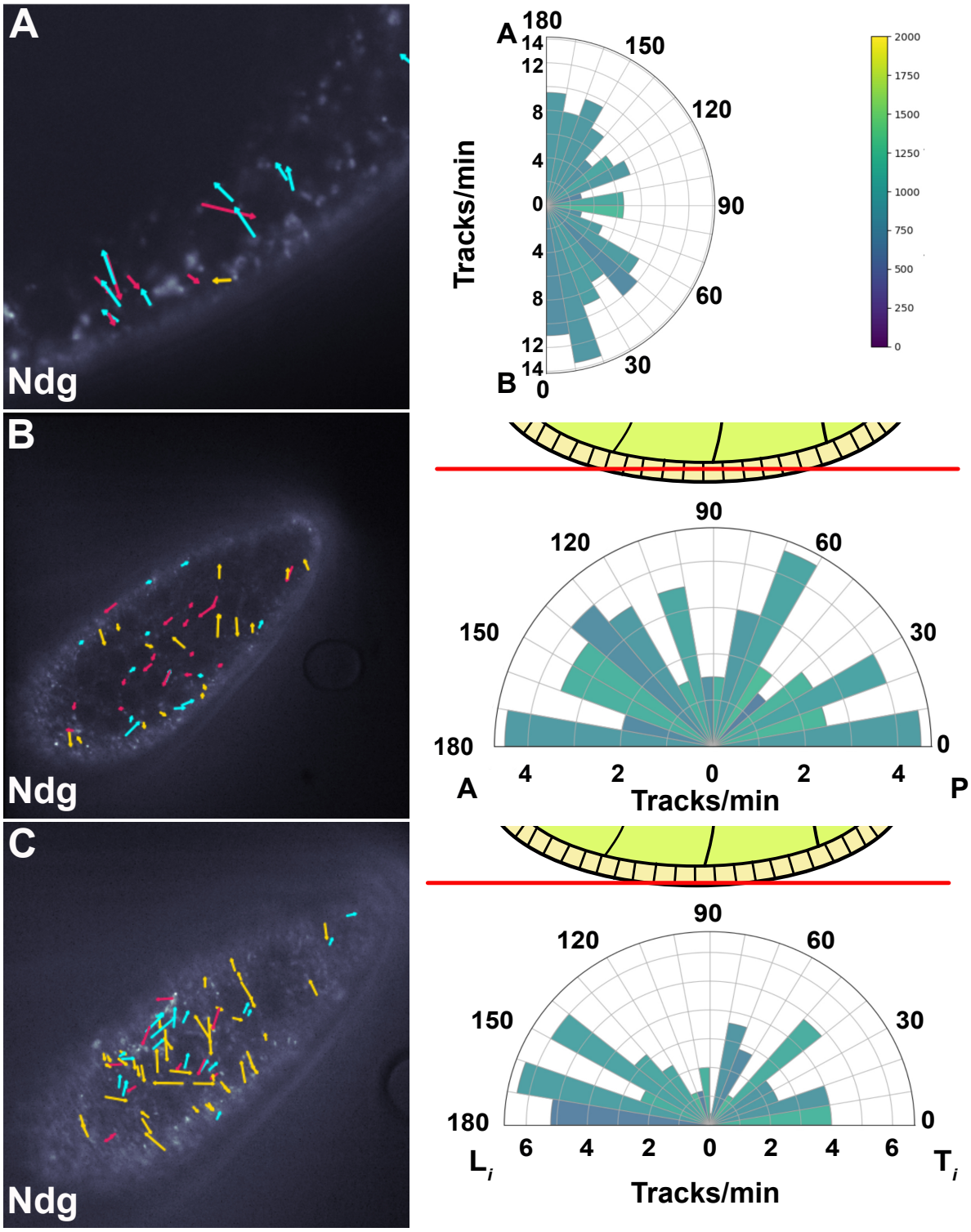

Supplement for Figure 6 – Spinning disc imaging of Nidogen trafficking

A) Tracks from representative movie taken on a spinning disc microscope of Ndg vesicle movements along the apical-basal axis of a stage 8 egg chamber. The polar plot on the right represents data from 2 spinning disc movies and shows a slight basal bias Ndg movements.

B) Tracks from representative movie taken on a spinning disc microscope of Ndg vesicle movements Ndg tracks in a transverse section through the middle section of the follicle cells (see diagram). The polar plot represents data from 3 spinning disc movies and shows no clear bias in track direction.

C) Tracks from representative movie taken on a spinning disc microscope of Ndg vesicle movements Ndg tracks in a transverse section at the basal side of the follicle cells (see diagram). The leading and trailing (L and T) directions of follicle cell migration are indicated in the polar plot on the right, which shows that most tracks are directed towards the leading edge.

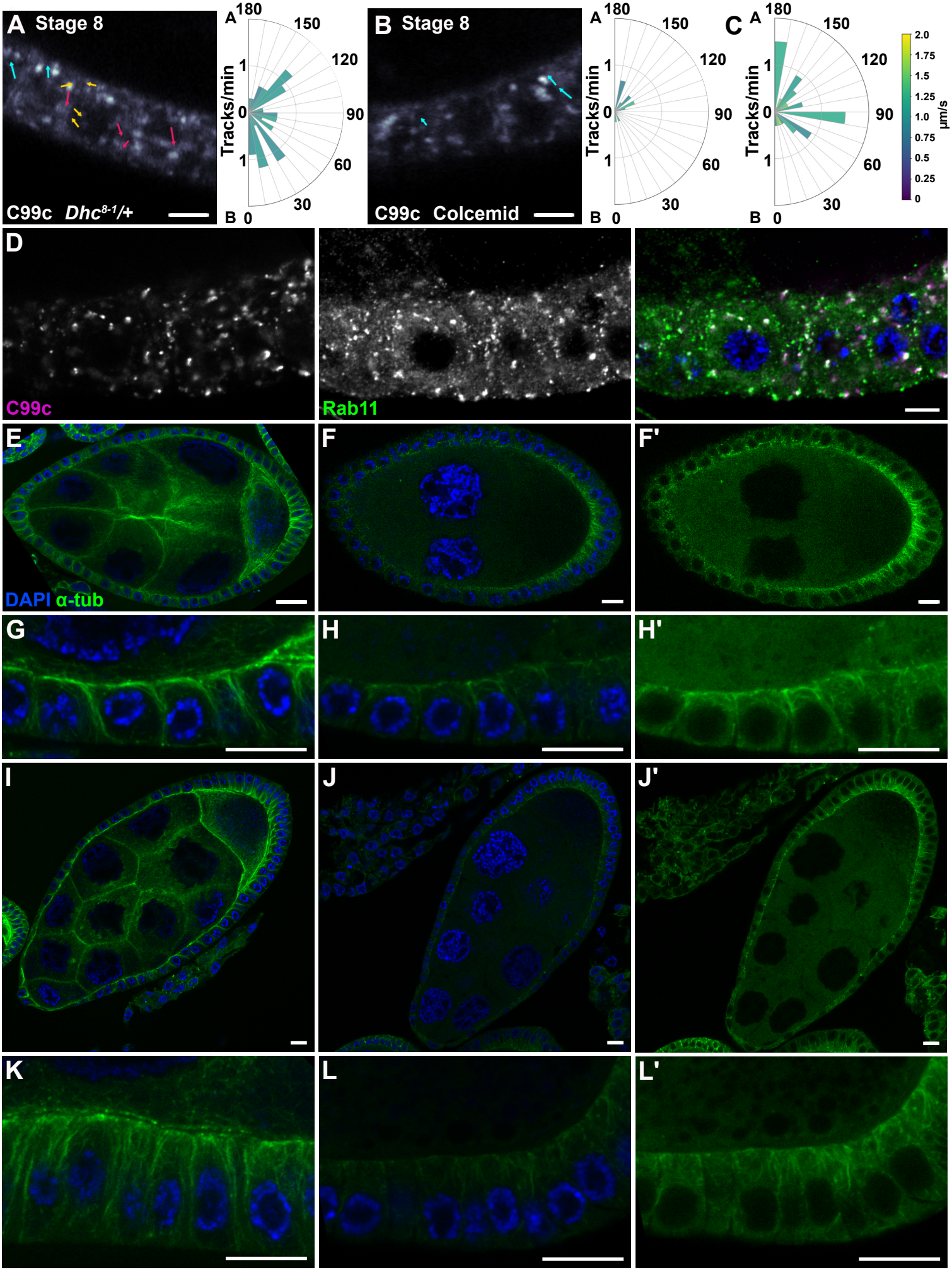
A Stage 8
C99c Dhc8-1/+
Tracks/min
B Stage 8
C99c Colcemid
C
µm/s
D
C99c
Rab11
E
DAPI α-tub
F
F'
G
H
H'
I
J
J'
K
L
L'

Supplement for Figure 8 – *Dhc*$^{8-1}$/+ and colcemid treatments.

A) Tracks from a representative movie of Cad99c trafficking in a *Dhc*$^{8-1}$ heterozygous stage 8 egg chamber 33 minutes after biotin addition. Scale bar 5 µm. The polar plot on the right represents data from 3 movies.

B) Tracks from a representative movie of Cad99c trafficking 24 minutes after biotin addition in a stage 8 egg chamber that has been treated with colcemid to depolymerise microtubules. Scale bar 5 µm. The polar plot on the right represents data from 4 movies

C) Polar plot representing data from 2 movies showing the number of Cad99c tracks per minute in wild-type stage 8 egg chambers.

Graph scales in A) B) and C) are the same to allow for easy comparison.

D) Rab11 and Cad99c localisation in colcemid-treated egg chambers 30 minutes after the addition of biotin. Rab11 positive recycling endosomes are no longer enriched apically and can be seen laterally and basally with Cad99c. Scale bar 5 µm.

E), G), I), K) β-tubulin staining in mock injected flies. Scale bar 10 µm.

F), H), J), L) β-tubulin staining in flies injected with colcemid. These images were collected with the same microscope settings and laser power colour scale as the mock injected images. Scale bar on 10 µm. F'), H'), J'), L') have all been adjusted to show the details of the remaining microtubules.

G) and H) show microtubules in stage 8 follicle cells.

K) and L) show microtubules in stage 9 follicle cells.

Cargo	Stage	No of Movies	Apical	Basal	Lateral	Total	% Apical	%Basal	%Lateral	Significance
C99c	8	3	9	5	15	29	31.03	17.24	51.72	ns
C99c	9	5	86	20	12	118	72.88	16.95	10.17	****
C99c Late	9	3	23	16	6	45	51.11	35.56	13.33	ns
C99c dhc8−1/+	8	3	7	12	15	34	20.59	35.29	44.12	ns
C99c dhc8−1/+	9	3	19	19	5	43	44.19	44.19	11.63	ns
C99c colcemid	8	4	6	2	3	11	54.55	18.18	27.27	ns
C99c colcemid	9	4	11	14	13	38	28.95	36.84	34.21	ns
Ndg	8	3	83	109	136	328	25.30	33.23	41.46	ns
Ndg dhc8−1/+	8	3	47	70	80	197	23.86	35.53	40.61	ns
			Leading	Trailing	Sideways	Total	% Leading	% Trailing	% Sideways	
Ndg basal	8	3	103	69	58	230	44.78	30.00	25.22	*
Ndg mid	8	3	110	88	134	332	33.13	26.51	40.36	ns
Ndg basal dhc8−1	8	2	90	76	84	250	36.00	30.40	33.60	ns
Rab10 alone	8	2	43	49	27	119	36.13	41.18	22.69	ns
Rab10 with Ndg	8	2	96	62	52	210	45.71	29.52	24.76	*
	Stage	No of Movies	Rab10 +ve	Rab10 −ve or unclear	Total	% Rab10 +ve				
Ndg	8	2	164	47	211	77.73				

Table S1

The number of vesicles travelling in each direction for all tracked RUSH movies of Cad99c and Ndg.

Chi^2 tests were performed to determine if the tracks were directionally biased. The null hypothesis was that equal numbers of tracks would travel apically/basally, or leading/trailing.